Hindawi
Shock and Vibration
Volume 2024, Article ID 7926619, 21 pages
https://doi.org/10.1155/2024/7926619

Research Article

Uncertainty Quantification of Vibroacoustics with Deep Neural Networks and Catmull–Clark Subdivision Surfaces

Zhongbin Zhou,[1,2] **Yunfei Gao**,[2] **Yu Cheng**,[2,3] **Yujing Ma**,[2,3] **Xin Wen**,[4] **Pengfei Sun**,[1] **Peng Yu**,[5] **and Zhongming Hu**[2]

[1]*Key Laboratory of In-Situ Property-Improving Mining of Ministry of Education, Taiyuan University of Technology, Taiyuan 030024, China*
[2]*Henan International Joint Laboratory of Structural Mechanics and Computational Simulation, School of Architectural Engineering, Huanghuai University, Zhumadian 463000, China*
[3]*College of Architecture and Civil Engineering, Xinyang Normal University, Xinyang 464000, China*
[4]*School of Software, Taiyuan University of Technology, Taiyuan 030024, China*
[5]*College of Civil Engineering and Architecture, Key Laboratory of Disaster Prevention and Structural Safety of Ministry of Education, Guangxi Key Laboratory of Disaster Prevention and Structural Safety, Guangxi University, Nanning 530004, China*

Correspondence should be addressed to Yunfei Gao; gbb304@163.com and Zhongming Hu; hu-zhongming@huanghuai.edu.cn

Received 29 September 2023; Revised 15 December 2023; Accepted 25 January 2024; Published 10 February 2024

Academic Editor: Arcanjo Lenzi

This study proposes an uncertainty quantification method based on deep neural networks and Catmull–Clark subdivision surfaces for vibroacoustic problems. The deep neural networks are utilized as a surrogate model to efficiently generate samples for stochastic analysis. The training data are obtained from numerical simulation by coupling the isogeometric finite element method and the isogeometric boundary element method. In the simulation, the geometric models are constructed with Catmull–Clark subdivision surfaces, and meantime, the physical fields are discretized with the same spline functions as used in geometric modelling. Multiple deep neural networks are trained to predict the sound pressure response for various parameters with different numbers and dimensions in vibroacoustic problems. Numerical examples are provided to demonstrate the effectiveness of the proposed method.

1. Introduction

Thin-shell structures manifest an evident vibroacoustic interaction phenomenon, which has a significant impact on structural safety and noise control. Considering the inherent randomness of material properties, geometry, and loading [1–7], it is necessary to quantify these uncertainties to evaluate structural reliability in engineering [8]. The commonly used uncertainty quantification methods include Monte Carlo simulation (MCs) [9–15], stochastic spectral methods [16, 17], and perturbation methods [18]. Among them, MCs is the most versatile and easiest to implement, but it requires a large number of samples to ensure sufficient accuracy [19]. Hence, MCs is feasible in practice only when simulation can be conducted very efficiently.

A surrogate model can accurately fit numerical calculation results and consume less computing power, thereby speeding up the sample generation process and alleviating the issue of inadequate samples during Monte Carlo simulation. Well-known surrogate models include radial basis functions (RBFs) [20–23], polynomial chaos expansions [24–26], Gaussian processes [27–30], and relevance vector machines [31, 32]. Each of these models has its own advantages and is widely used. Nonetheless, when the number of random variables increases, the effectiveness of these approaches significantly diminishes.

The state-of-the-art surrogate model, deep neural network (DNN), can effectively address the issue of excessive input dimensions. Huang [33] et al. conducted a comparative analysis for different regression surrogate models in energy transmission quality forecasting, which reveals that DNN serves as the most suitable regression model. Jung [34] et al. constructed a DNN surrogate model to predict propellant combustion characteristics, in which the high-dimensional inputs are captured throughout stochastic analysis. Kontou [35] et al. have effectively minimized the optimization turnaround time by employing DNN for turbulence closure in Reynolds-averaged Navier–Stokes equations. The results obtained by the DNN model agree well with the solution by classical numerical methods. Shahriari [36] et al. used DNN as a surrogate model of Maxwell's equations to infer geological conditions from resistivity. Sun [37] et al. used 15 input variables to estimate the variable infiltration capacity of soil moisture. Comparative analysis of models validates the superior performance of DNN. Moreover, many efforts are made to improving DNN by incorporating physical information [38–43].

In order to construct a reliable DNN model, high-quality training data should be generated from high-performance simulation. The finite element method (FEM) is a powerful method in vibration analysis. However, the boundary element method (BEM) is superior to FEM in calculating sound waves in exterior domains [44–49], as it discretizes only the structural surfaces without truncating the unbounded domain. Therefore, combining these two methods can significantly enhance calculation efficiency and accuracy [50]. Moreover, traditional FEM/BEM employs polygonal elements, which deteriorate geometric accuracy and lead to heavy meshing burden. The isogeometric analysis (IGA) [51–54] can address this challenge by integrating numerical analysis and computer-aided design (CAD). Coupling the FEM/BEM in the context of isogeometric analysis further improves the computing performance.

In this paper, a novel DNN-accelerated MCs framework is proposed for uncertainty quantification. Following the work of [55], the Catmull–Clark subdivison is applied as a surface refinement method. We add density and Young's modulus as independent variables in DNN inputs and expand the input dimension to 5 in calculation of a sphere model. We add density, Young's modulus, and Poisson ratio in the analysis of the submarine model. As shown in Figure 1, the method is mainly comprised of two parts. The first part is isogeometric FEM/BEM, which simulates vibroacoustic systems from the geometric model of Catmull–Clark subdivision surfaces. The simulation results provide training data for DNN. It is noted that compared to loop subdivision surfaces as used in [55], the Catmull–Clark subdivision surface allows for quadrilateral elements. The second part of the uncertainty analysis framework is that DNN is employed as a surrogate model to rapidly generate samples for MCs. Multiple DNN models are created due to different types of input variables, and the statistical indicators of MCs include expectation and standard deviation.

The remainder of this paper is as follows: Section 2 describes MCs and presents the physics problem. Section 3 describes a brief DNN theory. Section 4 presents the IGA FEM/BEM with the Catmull–Clark subdivision surface. Section 5 applies sphere and submarine models to verify the proposed method. Finally, in Section 6, the conclusion is provided.

2. MCs and Structureacoustic Coupling Problems

The Monte Carlo simulation (MCs) can learn about a system through a large number of random samples affected by stochastic parameters. By calculating statistics, for example, expectation and standard deviation, MCs can be applied to stochastic analysis, which is shown as follows:

$$\mathrm{E} \approx \frac{1}{N} \sum_{\ell=1}^{N} f\left(\mathbf{x}^{\ell}\right), \tag{1}$$

$$\mathrm{D} \approx \frac{1}{N-1} \sum_{\ell=1}^{N} \left(f\left(\mathbf{x}^{\ell}\right) - E\right)^2, \tag{2}$$

where N is the number of samples, $\mathbf{x}$ is the independent variable, and ℓ denotes the ℓ-th sample.

In general, MCs mainly consists of the following four processes:

(1) Determine the physics problem and its influencing factors

(2) Collect or generate sample data through various means

(3) Calculate the physical responses of each sample point

(4) Calculate statistical indicators for uncertainty quantification

The MCs is suitable for multidimensional input problems and less limited by geometric conditions. Its convergence speed is independent of the dimension, and errors are easy to determine. Thus, it is suitable for stochastic analysis of vibroacoustic coupling problems. The mathematical model of the problem is shown in Figure 2. In the figure, Ω_s is the thin-shell structure, Ω_f is the fluid domain, and $\Gamma = \Omega_s \cap \Omega_f$ is the coupling surface. The Kirchhoff–Love shell theory and the Helmholtz equation are used as a governor for thin-shell mechanical behavior and radiation or scattered acoustic field, respectively.

We consider the input plane wave or a time-harmonic force with an angular frequency ω and use subscript (x) as random parameters. It is essential to solve the following coupled equations [56, 57]:

$$\nabla \cdot \sigma_{(x)} + \omega^2 \rho_s \mathbf{u}_{(x)} = 0, \text{in } \Omega_s, \tag{3}$$

$$\nabla^2 p_{(x)} + k^2 p_{(x)} = 0, \text{in } \Omega_f, \tag{4}$$

$$\sigma_{(x)} \cdot \mathbf{n}_s + p_{(x)} = 0, \text{on } \Gamma, \tag{5}$$

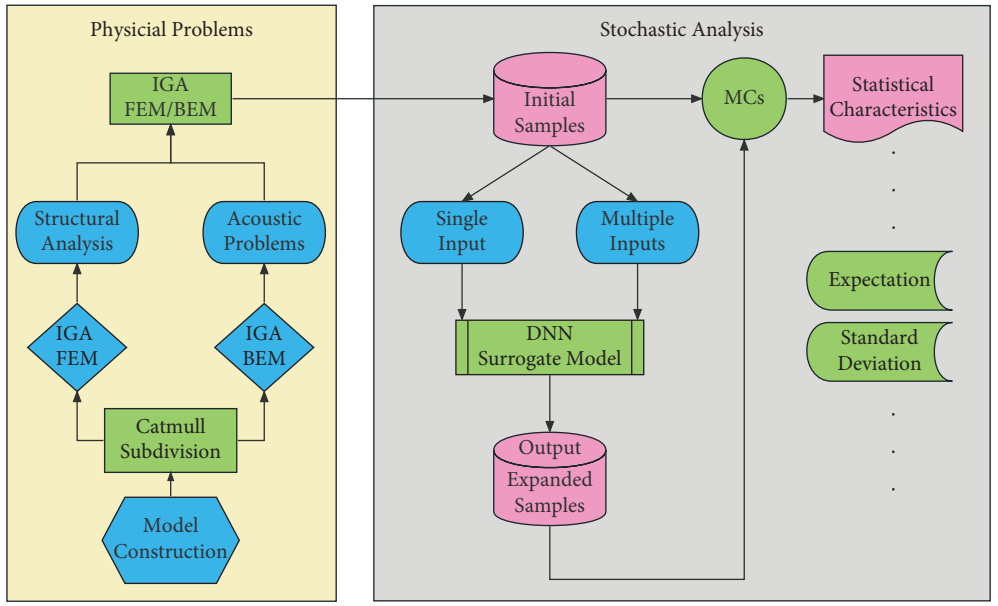

Figure 1: DNN-accelarated MCs process.

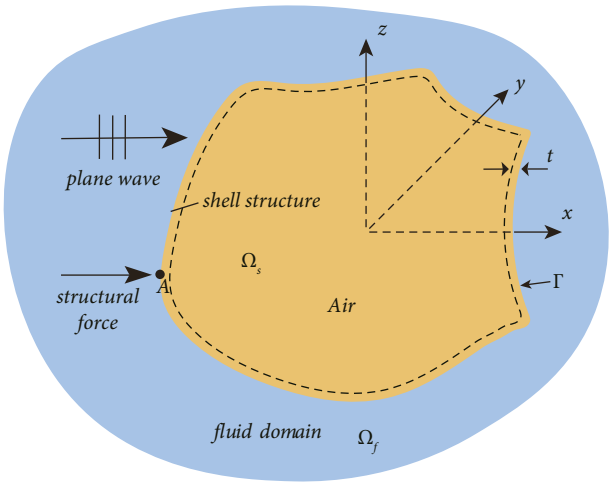

Figure 2: Mathematical model of acousticvibration coupling problem.

$$\omega \mathbf{u}_{(x)} \cdot \mathbf{n}_f = v, \text{on } \Gamma, \tag{6}$$

where equations (3) and (4) are the governing equations, (5) and (6) represent force balance and displacement continuity, ∇, $\boldsymbol{\sigma}_{(x)}$, and $\mathbf{u}_{(x)}$ are the Laplace operator, stress tensor, and displacements, respectively, ρ_s, $p_{(x)}$, and v are the density, the sound pressure, and the the fluid normal velocity, $\mathbf{n}_s$ and $\mathbf{n}_f$ are the normal vectors, and $i = \sqrt{-1}$ and k are the imaginary unit and the wave number, respectively.

Before presenting the specific numerical calculation methods, we will show how to calculate the statistical characteristics of responses.

Let $\mathcal{X}$ denote the random variables, which is

$$\mathcal{X} = \left\{ \{x_1, x_2, \cdots, x_n\} \middle| x_i \in [x_{\min}, x_{\max}] \right\}, \quad i = 1, \cdots, n, \tag{7}$$

where $x_{\min}$ and $x_{\max}$ are input bounds and n is the input dimension. We select N values from $\mathcal{X}$ to form samples $\mathbf{X} \in \mathbb{R}^N$, that is

$$\mathbf{X} = \left\{ \mathbf{x}^\ell \middle| \mathbf{x}^\ell \in \mathcal{X} \right\}, \quad \ell = 1, \cdots, N, \tag{8}$$

where $\mathbf{x} = [x_1, \cdots, x_n]^T$. Then, utilizing IGA FEM/BEM, the response $\mathbf{Y} = [y_1, \cdots, y_m]^T$ of each point $\mathbf{x}$ can be evaluated as follows:

$$\mathbf{Y} = \left\{ f\left(\mathbf{x}^\ell\right) \middle| \mathbf{x}^\ell \in \mathcal{X} \right\}, \quad \ell = 1, \cdots, N. \tag{9}$$

Finally, the dataset can be generated by assembling $\mathbf{X}$ and $\mathbf{Y}$ as follows:

$$\left\{ \left(\mathbf{x}^1, \mathbf{Y}^1\right), \cdots, \left(\mathbf{x}^\ell, \mathbf{Y}^\ell\right), \cdots \left(\mathbf{x}^N, \mathbf{Y}^N\right) \right\}. \tag{10}$$

Although MCs has numerous advantages, its accuracy heavily relies on the number of samples, which results in significant wastage of computing resources. With complexity and influencing factors increasing, numerical calculations become highly time-consuming and put a heavy burden on computer performance. Furthermore, to maintain the accuracy of stochastic analysis, increasing the number of sampling points becomes necessary, which makes it challenging to obtain the response merely through numerical simulation. Therefore, a cost-effective and time-efficient method is required to overcome this drawback.

3. DNN Surrogate Model

As mentioned previously, the process of finding solutions for all samples in Monte Carlo simulation is typically time-consuming and requires significant computing power. Thus, to solve this problem, in this section, we propose a DNN surrogate model to accelerate stochastic analysis. It can

enlarge the initial dataset of N_I generated by numerical calculations to dataset of N_L as follows:

$$\left\{\left(\mathbf{X}^1, \mathbf{Y}^1\right), \cdots, \left(\mathbf{X}^{\ell}, \mathbf{Y}^{\ell}\right), \cdots \left(\mathbf{X}^{N_I}, \mathbf{Y}^{N_I}\right)\right\} \longrightarrow \left\{\left(\mathbf{X}^1, \mathbf{Y}^1\right), \cdots, \left(\mathbf{X}^{\ell}, \mathbf{Y}^{\ell}\right), \cdots \left(\mathbf{X}^{N_L}, \mathbf{Y}^{N_L}\right)\right\}. \tag{11}$$

Now, let us provide a brief introduction for DNN (please see [58–61] for detailed information). By utilizing a specific mapping function f, DNN can use input of multitype and any amount to predict output of multitype and any amount. To acquire a best f, the original DNN model needs to be trained, and this process is usually guided by the loss function. Assuming that the initial dataset with N_I samples is the training dataset, in which $\mathbf{X}^{\ell} = (x_1^{\ell}, x_2^{\ell}, \cdots, x_n^{\ell})^T$ is the input data, $\mathbf{Y}^{\ell} = (y_1^{\ell}, y_2^{\ell}, \cdots, y_m^{\ell})^T$ is the real value (target) needed to be compared with predictions (outputs). After training, the best model can then use larger amounts of inputs to generate corresponding outputs, which is the process of expansion of the initial dataset for MCs.

Moreover, a general DNN model is shown in Figure 3. According to it, let $\mathbf{X}^{\ell}$, H^n, and $\mathbf{Y}^{\ell}$ denote the vector of input layer, hidden layer, and output layer, respectively, the forward calculation process of DNN can be expressed by following equations:

$$\begin{cases} h_{j_1}^1 = \hat{f}\left(\sum_{i=1}^{s_0} w_{ij_1}^1 \cdot x_i^{\ell} + b_{j_1}^1\right), & j_1 = 1, 2, \cdots, s_1, \\ h_{j_n}^n = \hat{f}\left(\sum_{i=1}^{s_{n-1}} w_{ij_n}^n \cdot h_i^{n-1} + b_{j_n}^n\right), & j_n = 1, 2, \cdots, s_n, n = 1, 2, \cdots, m, \\ y_k^{\ell} = \hat{f}\left(\sum_{i=1}^{s_m} w_{ik}^{m+1} \cdot h_i^m + b_k^{m+1}\right), & k = 1, 2, \cdots, s_{m+1}, \end{cases} \tag{12}$$

where w and b are the weights and bias of linear transformation between layers and s, m, and $\hat{f}$ are the number of neurons, number of hidden layers, and activation function, respectively.

The response predicting by DNN of the vibroacoustic problem is a regression process. The mean square error (MSE) is a typical loss function for this process. Assuming that the prediction is $\hat{y}_i^{\ell}$ (i for i-th unit), MSE is as follows:

$$\text{Loss} = \frac{1}{N_I} \sum_{\ell=1}^{N_I} \sum_{i=1}^{m} \left(\hat{y}_i^{\ell} - y_i^{\ell}\right)^2. \tag{13}$$

By selecting an appropriate learning rate, the optimal weights w and biases b can be acquired through a chosen optimizer. It is difficult to fully evaluate the performance of the DNN model from all perspectives with a single evaluation metric. Therefore, additional metrics such as RMSE (root mean squared error), MAE (mean absolute error), and MAPE (mean absolute percentage error) are introduced to assess the performance of the trained model, which are

$$\text{RMSE} = \frac{1}{N_{\text{test}}} \sum_{\ell=1}^{N_{\text{test}}} \sqrt{\frac{1}{n} \sum_{i=1}^{n} \left(\hat{y}_i^{\ell} - y_i^{\ell}\right)^2}, \tag{14}$$

$$\text{MAE} = \frac{1}{N_{\text{test}}} \sum_{\ell=1}^{N_{\text{test}}} \frac{1}{n} \sum_{i=1}^{n} \left|\hat{y}_i^{\ell} - y_i^{\ell}\right|, \tag{15}$$

$$\text{MAPE} = \frac{1}{N_{\text{test}}} \sum_{\ell=1}^{N_{\text{test}}} \frac{100\%}{n} \sum_{i=1}^{n} \frac{\left|\hat{y}_i^{\ell} - y_i^{\ell}\right|}{\left|y_i^{\ell}\right|}, \tag{16}$$

where $\hat{y}_i$ and y_i are the prediction and the real value, respectively, and n and N_{test} are the number of testing points and testing data, respectively.

By employing both MAE and RMSE, one can assess the extent of dispersion of sample error. Likewise, when using MAPE and MAE in conjunction with the average value of prediction, the fitting accuracy across samples of varying magnitudes can be evaluated. More clearly, a DNN-based stochastic analysis process is illustrated in Figure 4. The steps in the figure can be concluded into following three parts:

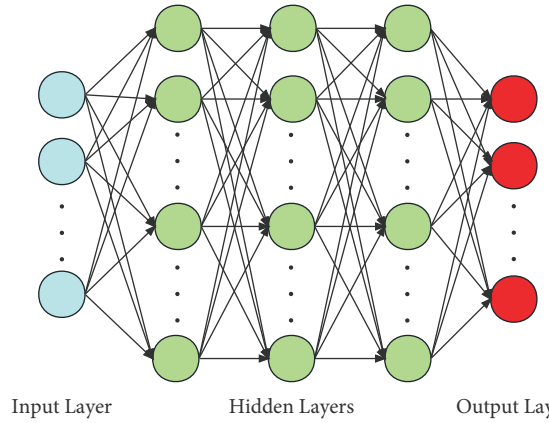

Figure 3: Deep neural network structure.

(i) Dataset preparation: Using statistical data to standardize the dataset $(\mathbf{X}^{\ell}, \mathbf{Y}^{\ell})$,

$$S_{x_i^{\ell}} = \frac{x_i^{\ell} - \hat{\mu}_i}{\hat{\sigma}_i},$$
$$S_{y_j^{\ell}} = \frac{y_j^{\ell} - \breve{\mu}_j}{\breve{\sigma}_j}, \quad (\ell = 1, \cdots, N_I;\ i = 1, \cdots, n;\ j = 1, \cdots, m), \tag{17}$$

where x_i^{ℓ} and y_j^{ℓ} represent the input and output of $(\mathbf{X}^{\ell}, \mathbf{Y}^{\ell})$, respectively, the corresponding $S_{x_i^{\ell}}$ and $S_{y_j^{\ell}}$ denote the standardized value, $\hat{\mu}_i$ and $\hat{\sigma}_i = \hat{\mu}_i \times \hat{\gamma}_i$ denote the mean value and standard deviation of inputs, and $\hat{\gamma}_i$ is the coefficient of variation. Meanwhile, $\breve{\mu}_j$ and $\breve{\sigma}_j$ are the mean value and the standard deviation of outputs. Finally, the exact dataset can be rewritten as

$$\{(S_{\mathbf{X}^1}, S_{\mathbf{Y}^1}), \cdots, (S_{\mathbf{X}^{\ell}}, S_{\mathbf{Y}^{\ell}}), \cdots (S_{\mathbf{X}^{N_I}}, S_{\mathbf{Y}^{N_I}})\}. \tag{18}$$

(ii) Training and testing: The dataset in equation (18) is divided into two groups for training and testing. The mapping function f is acquired through the training dataset, and then, the testing dataset is used to assess the trained model. Finally, postprocessing of $\hat{y}_j^{\ell}$ is conducted, which is as follows:

$$\text{Post}_{\hat{y}_j^{\ell}} = \hat{y}_j^{\ell} \times \breve{\sigma}_j + \breve{\mu}_j, \quad (j = 1, \cdots, m), \tag{19}$$

where $\text{Post}_{\hat{y}_j^{\ell}}$ denotes the j-th postprocessed value, $\hat{y}_j^{\ell}$ denotes the initial output of the DNN model, and $\breve{\mu}_j$ and $\breve{\sigma}_j$ are priori data in equation (17).

(iii) Application: After the function f has been constructed, it can be used to predict the responses $S_{\tilde{\mathbf{Y}}}$ using existing or randomly generated data as inputs $S_{\mathbf{X}} \in \mathbb{R}^n$. Then, postprocessing should be conducted to get the meaningful value. Finally, the dataset with N_I samples obtained by numerical calculations is enlarged to one with N_L samples generated by DNN through the above operations.

4. IGA FEM/BEM with Catmull–Clark Subdivision Surfaces

In order to obtain the initial samples of good quality for DNN training, it is necessary to choose an appropriate numerical calculation method. In this work, IGA FEM/BEM with the Catmull–Clark subdivision surface method is introduced to acquire responses of random generated samples. In the following subsections, the Catmull–Clark subdivision surfaces will be introduced first; then, IGA FEM and IGA BEM methods are demonstrated, respectively. Finally, the coupled method is presented.

4.1. Catmull–Clark Subdivision Surface Scheme. The subdivision surface method has drawn significant attention due to its effectiveness in shaping smooth limit surfaces. Moreover, the compatibility of the subdivision surface method with the shell finite element method or the boundary element method is natural since they all focus on the structural surface. The Catmull–Clark subdivision surface method is one of the self-adaptive mesh technologies. Compared to other similar methods, it can maintain structural model consistency with no geometric model error

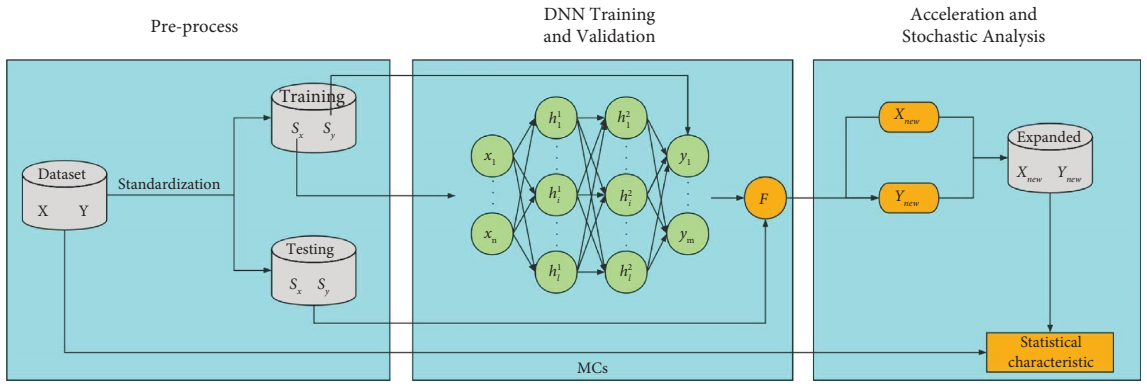

Figure 4: Flow of DNN-based stochastic analysis.

during automatic mesh refinement (increasing the mesh number). Thus, the Catmull–Clark subdivision algorithm with the bicubic B-spline is applied to refine the control meshes.

The subdivision process divides each element into four subquadrilateral elements, as illustrated in Figure 5. The refinement of the quadrilateral mesh can be seen in Figure 6. To explain its rules, let us assume the initial mesh subdivision level k, and after one subdivision, it becomes the level $k+1$. The vertices denoted by "V" on the k level are weighted to determine the $k+1$-level vertices. At each element, four new vertices are inserted at the middle of edges, denoted by "E." In addition, a new vertex is inserted at the center of the k-level element, denoted by "F." The edge passing through "V" on the k level is the adjacent edge. The valence n_v of a vertex represents the number of adjacent edges. A vertex is classified as a regular vertex if $n_v = 4$; otherwise, it is an irregular vertex, as shown in Figure 7. The interpolation weights are illustrated in Figure 6.

To build smooth surfaces, bicubic box splines are applied. The patch of a regular element contains 16 vertices (Figure 7). The shape of the mapped surface is expressed as follows [62]:

$$X(\alpha_1, \alpha_2) = \sum_{i=1}^{16} B_i(\alpha_1, \alpha_2) x_i, \tag{20}$$

where X is the point coordinates, (α_1, α_2) is its parameter coordinate, B_i is the basis function, and x_i is the control vertex coordinate. Detailed formulas for B_i can be found in [62].

Figure 8 shows how to deal with irregular elements, and the fitting point will finally be located in regular subelements after a limited number of subdivisions. Then, equation (20) can be used to acquire the shape of the mapped surface.

4.2. IGA FEM with Catmull–Clark Subdivision Surfaces. According to the Kirchhoff–Love shell theory, the thin-shell variational formulation can be written as follows [57, 63]:

$$\delta W = \delta W_v + \delta W_i + \delta W_e = 0, \tag{21}$$

where the three terms δW_v, δW_i, and δW_e are the virtual work contributions, internal, and external forces, respectively. If the midsurface displacements $\mathbf{u}$ are time harmonic, they can be rewritten as

$$\begin{aligned}
\delta W_v &= -\omega^2 \int_\Gamma \rho_s t \mathbf{u} \cdot \delta \mathbf{u} \mathrm{d}\Gamma, \\
\delta W_i &= \int_\Gamma \left(\frac{1}{2} \frac{\mathrm{Et}}{1-\nu^2} \delta \boldsymbol{\varepsilon}^{\mathrm{T}} \mathbf{C} \boldsymbol{\varepsilon} + \frac{1}{2} \frac{Et^3}{12\left(1-\nu^2\right)} \delta \boldsymbol{\kappa}^{\mathrm{T}} \mathbf{C} \boldsymbol{\kappa} \right) \mathrm{d}\Gamma, \\
\delta W_e &= -\int_\Gamma p \mathbf{n}_s \cdot \delta \mathbf{u} \mathrm{d}\Gamma,
\end{aligned} \tag{22}$$

where $\mathbf{C}$ is material constants, E, ν, and t are Young's modulus, Poisson ratio, and the shell thickness, respectively, $\boldsymbol{\varepsilon}$ and $\boldsymbol{\kappa}$ are the membrane and bending strains, respectively, and Γ is the boundary.

After the governor equation is determined, the Catmull–Clark subdivision surface is introduced to FEM [64]. To discrete the displacement, the basis functions $B(\alpha_1, \alpha_2)$ are used as follows:

$$\mathbf{u} = \sum_{i=1}^{2\nu+8} B_i(\alpha_1, \alpha_2) \mathbf{u}_i, \tag{23}$$

where u_i is the nodal parameter. Therefore, after element matrices are assembled, the equations system is as follows:

$$\mathbf{A}\mathbf{u} = \mathbf{f}, \tag{24}$$

where $\mathbf{A} = \mathbf{K} - \omega^2 \mathbf{M}$ is the coefficient matrix of FEM, $\mathbf{K}$ and $\mathbf{M}$ are the stiffness matrix and mass matrix, $\mathbf{u}$ is the displacement, and the load $\mathbf{f}$ is the sum of $\mathbf{f}_m$ (the mechanical force) and $\mathbf{f}_s$ (the sound pressure load) as follows:

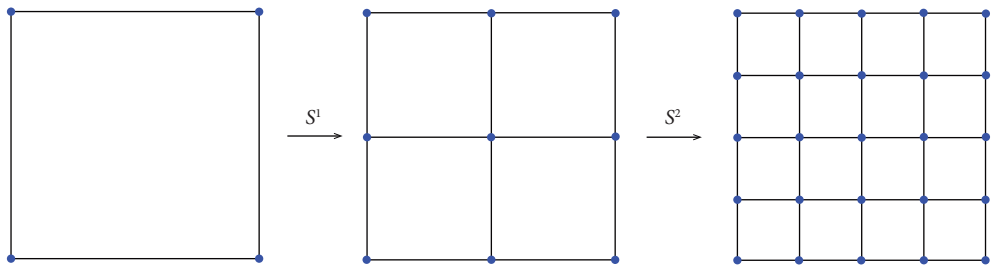

Figure 5: Catmull–Clark subdivision process.

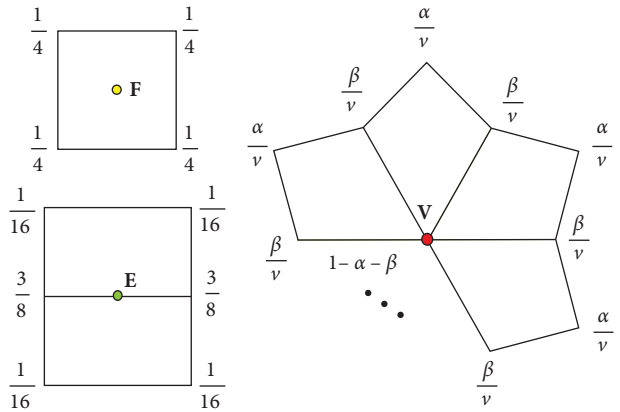

Figure 6: Interpolation weights of origin vertices to vertices "F," "E," and "V" (see [62]).

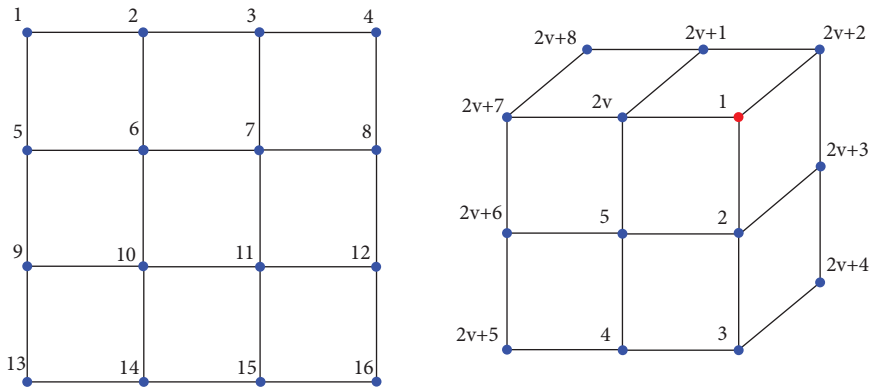

Figure 7: The subdivision surface vertices (the irregular one is marked red).

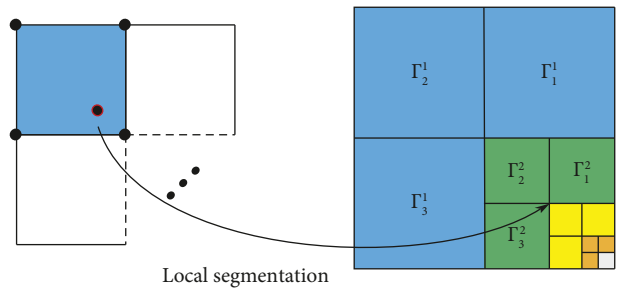

Figure 8: Surface fitting for irregular elements (see [62]).

$$\mathbf{f} = \mathbf{f}_m + \mathbf{f}_s. \tag{25}$$

4.3. IGA BEM with Catmull–Clark Subdivision Surfaces. Based on the Burton–Miller formulation, Helmholtz equation (4) can be transformed to the following boundary integral equation [65–69]:

$$C(x)[p(x) + \delta q(x)] + (H^* p)(x) + \delta\left(\widetilde{H}^* p\right)(x) = (G^* q)(x) + \delta\left(\widetilde{G}^* q\right)(x) + p_{\text{inc}}(x) + \delta\widetilde{p}_{\text{inc}}(x), \tag{26}$$

where $\delta = i/k$ (for $k > 1$) is the combining parameter, $C(x)$ is the jump term, p_{inc} is the acoustic pressure of the incident wave, q and $\widetilde{p}_{\text{inc}}$ are the normal derivative of p and p_{inc}, respectively, and G^*, H^*, $\widetilde{G}^*$, and $\widetilde{H}^*$ are the boundary integral operators, which are as follows:

$$\begin{aligned}
(G^* q)(x) &\coloneqq \int_\Gamma G(x,y) q(y) \mathrm{d}\Gamma(y),\\
(H^* p)(x) &\coloneqq \int_\Gamma \frac{\partial G(x,y)}{\partial n(y)} p(y) \mathrm{d}\Gamma(y),\\
\left(\widetilde{G}^* q\right)(x) &\coloneqq \int_\Gamma \frac{\partial G(x,y)}{\partial n(x)} q(y) \mathrm{d}\Gamma(y),\\
\left(\widetilde{H}^* p\right)(x) &\coloneqq \int_\Gamma \frac{\partial^2 G(x,y)}{\partial n(x)\partial n(y)} p(y) \mathrm{d}\Gamma(y),
\end{aligned} \tag{27}$$

where $n(x)$ and $n(y)$ are unit outward normal, respectively. $G(x, y)$ (Green's function) and the derivative are defined as follows:

$$\begin{aligned}
G(x,y) &= \frac{e^{\mathrm{ikr}}}{4\pi r},\\
\frac{\partial G(x,y)}{\partial n(y)} &= -\frac{e^{\mathrm{ikr}}}{4\pi r^2}(1 - \mathrm{ikr})\frac{\partial r}{\partial n(y)},\\
\frac{\partial G(x,y)}{\partial n(x)} &= -\frac{e^{\mathrm{ikr}}}{4\pi r^2}[\mathrm{ikr} - 1]\frac{\partial r}{\partial n(x)},\\
\frac{\partial^2 G(x,y)}{\partial n(x)\partial n(y)} &= \frac{e^{\mathrm{ikr}}}{4\pi r^3}\left[(1 - \mathrm{ikr}) n_j(x) n_j(y) + \left(3 - 3\mathrm{ikr} - k^2 r^2\right)\frac{\partial r}{\partial n(x)}\frac{\partial r}{\partial n(y)}\right],
\end{aligned} \tag{28}$$

where $r = |x - y|$.

Then, the boundary is discreted by quadrilateral elements and constructed by IGA principles. In this work, the applications of basis functions of the Catmull–Clark subdivision surface are as follows:

$$p^e = \sum_{i=1}^{2v+8} B_i(\alpha_1, \alpha_2) p_i,$$
$$q^e = \sum_{i=1}^{2v+8} B_i(\alpha_1, \alpha_2) q_i, \tag{29}$$

where p and q are sound pressure and normal flux and subscripts e and i are for the element and node. Afterwards, the following equation is assigned to a collection of collocation points, which are

$$\begin{aligned} C(x)[p(x) + \delta q(x)] = {} & p_{\text{inc}}(x) + \delta \widetilde{p}_{\text{inc}}(x) + \sum_{e=1}^{N_e} \sum_{i=1}^{2v+8} q_i \int_{\Gamma_e} B_i(\alpha_1, \alpha_2) G(x, y(\alpha_1, \alpha_2)) \mathrm{d}\Gamma \\ & - \sum_{e=1}^{N_e} \sum_{i=1}^{2v+8} p_i \int_{\Gamma_e} B_i(\alpha_1, \alpha_2) \frac{\partial G(x, y(\alpha_1, \alpha_2))}{\partial n(y(\alpha_1, \alpha_2))} d\Gamma \\ & + \delta \sum_{e=1}^{N_e} \sum_{i=1}^{2v+8} q_i^e \int_{\Gamma_e} B_i(\alpha_1, \alpha_2) \frac{\partial G(x, y(\alpha_1, \alpha_2))}{\partial n(x)} \mathrm{d}\Gamma \\ & - \delta \sum_{e=1}^{N_e} \sum_{i=1}^{2v+8} p_i^e \int_{\Gamma_e} B_i(\alpha_1, \alpha_2) \frac{\partial^2 G(x, y(\alpha_1, \alpha_2))}{\partial n(x) \partial n(y(\alpha_1, \alpha_2))} \mathrm{d}\Gamma, \end{aligned} \tag{30}$$

where the quantity N_e represents the element number. The placement is acquired through fitting operations. Moreover, by gathering the equations for all collocation points and presenting them in matrix form, the linear system of equations can be obtained, which is as follows:

$$\mathbf{Hp} = \mathbf{Gq} + \mathbf{p}_{\text{inc}}, \tag{31}$$

where $\mathbf{H}$ and $\mathbf{G}$ are the coefficient matrices, $\mathbf{p}$ and $\mathbf{q}$ are the sound pressure and its flux, respectively, and $\mathbf{p}_{\text{inc}}$ is the incident wave.

It should be emphasized that solving equation (30) directly using the Gaussian quadrature method can be challenging as a result of singular integrals present in the equation. Thus, we use the regularization technique to deal with the problem. For more detailed information, please refer to [70].

4.4. IGA FEM/BEM with Catmull–Clark Subdivision Surfaces. Since $\mathbf{u}$, $\mathbf{p}$, $\mathbf{f}_p$, and $\mathbf{q}$ are unknown, equations (24) and (31) cannot be solved individually. They can be bond together through the boundary conditions in equations (5) and (6). In addition, the nodal force in equation (25) is related to $\mathbf{p}$ as follows:

$$\mathbf{f}_p = \mathbf{n}_f \, \Theta \, \mathbf{p}, \tag{32}$$

where $\Theta = \int_\Gamma \mathbf{B}^T \mathbf{B} \mathrm{d}\Gamma$, $\mathbf{B}$ is the global vector, and $\mathbf{n}_f$ is the normals matrix which is defined as [57, 63]:

$$\mathbf{n}_f = \begin{Bmatrix} n_1 \cdot e_1 & 0 & \cdots \\ n_1 \cdot e_2 & 0 & \cdots \\ n_1 \cdot e_3 & 0 & \cdots \\ 0 & n_2 \cdot e_1 & \cdots \\ 0 & n_2 \cdot e_2 & \cdots \\ 0 & n_2 \cdot e_3 & \cdots \\ \cdots & \cdots & \cdots \end{Bmatrix}, \tag{33}$$

where e_1, e_2, e_3 are the orthogonal normal Cartesian base vectors. Therefore, the new expression of equation (25) can be acquired through equation (32) as follows:

$$\mathbf{f} = \mathbf{Np} + \mathbf{f}_s, \tag{34}$$

where $\mathbf{N} = \mathbf{n}_f \Theta$.

Substituting equation (34) into equation (24), the structural system equation can be expressed as follows:

$$\mathbf{Au} = \mathbf{Np} + \mathbf{f}_s, \tag{35}$$

$\mathbf{q}$ (sound flux) in equation (31) is given as $\mathbf{q} = \omega^2 \rho_f \mathbf{N}^T \mathbf{u}$, where ρ_f is the fluid density and $\mathbf{N}^T = \mathbf{n}_f^T$. Then, equation (31) can be rewritten as

$$\mathbf{Hp} = \mathbf{G} \omega^2 \rho_f \mathbf{N}^T \mathbf{u}. \tag{36}$$

Substituting equation (35) into equation (36), the displacement $\mathbf{u}$ can be eliminated; then, the boundary element formulation is as follows [57, 63]:

$$[\mathbf{H} - \mathbf{GY}]\mathbf{p} = \mathbf{Gq}_s, \tag{37}$$

with

$$\begin{aligned} \mathbf{Y} &= \omega^2 \rho_f \mathbf{N}^T \mathbf{A}^{-1} \mathbf{N}, \\ \mathbf{q}_s &= \omega^2 \rho_f \mathbf{N}^T \mathbf{A}^{-1} \mathbf{f}_s. \end{aligned} \tag{38}$$

In this work, direct computation of the inverse matrix $\mathbf{A}$ in equation (38) is avoided due to its high time complexity. Instead, the solution of $\mathbf{A}^{-1}\mathbf{f}_s$ can be obtained by directly solving the algebraic equation $\mathbf{Ax} = \mathbf{f}_s$.

An important drawback of the boundary element method is the formation of $\mathbf{H}$ and $\mathbf{G} \in \mathbb{C}^{N\times N}$, which leads to $O(N^2)$ algorithmic operations when the number of degrees of freedom N is large. In this work, the FMM is utilized to address this issue for its low memory consumption and high accuracy. In addition, to further improve the speed of the algorithmic operations, a multipole expansion formulation based on partial wave expansion with rotation-coaxial translation is implemented. The original boundary integral can be divided into two parts: the near and the far field. The former is computed using the boundary element method (BEM), while the latter is computed using the accelerated BEM based on the fast multipole method (FMBEM). For more detailed information about the FMM, please refer to [70–73].

5. Calculation Examples for Verification

5.1. Verification of IGA FEM/BEM. In this section, a series of spherical models are used to validate the numerical simulation algorithm. The model is present in Figure 9. The external effect is incident plane waves with amplitude 1. The IGA FEM/BEM method is employed to handle the problem, and the obtained solution is compared with the analytical one. We use 6×6 and 10×10 Gaussian quadrature points for regular and singular integrals, respectively.

Figure 10 shows the results of sound pressure calculated with different variables and frequency at the computing point located on the fluid domain. Table 1 displays the variable settings for each case, where each case has a different variable value relative to Case 1. In Figure 10, the symbol "Simulation" represents the IGA FEM/BEM solution and "Analysis" represents the analytical solution. All calculations are performed in the lower frequency band, such as $f = 50, 150, 300$ Hz. Since the error becomes larger at higher frequencies (for details, see [55]), the high frequency cases are not considered in this work.

Observing the figure, it can be found that the two solutions exhibit a high level of agreement, which provides evidence for the effectiveness of the proposed method. The deviations at some certain frequencies like $f = 150$ Hz are caused by nonunique solutions, and the details can also be seen in [55]. In addition, with the change of different variables, the change trend of sound pressure as well as the peak position and occurrence times will change. In comparison, the radius and Young's modulus have a more substantial impact on sound pressure values, while other parameters have an impact that is less apparent. Sound pressure cloud diagrams are given in Figure 11. The figure once again confirms that different random parameters have a significant impact on the sound pressure value and its distribution.

In order to get further information about the specific evolution trends of sound pressure with different variables, analytical calculations and numerical calculations are conducted employing the radius and other variables as independent variables. Figures 12 and 13 illustrate the sound pressure changes with different variables at the fixed calculating point (5, 0, 0). It shows that there is a decreasing trend of sound pressure with radius increasing, while with other variables increasing, the sound pressure is growing as a whole. Due to the strong correlation between sound pressure and shown variables, it is worth using these variables to perform stochastic analysis of sound pressure. At the same time, it can also be found that the results of numerical simulation and theoretical analysis are still in agreement with different independent variables.

5.2. DNN-MCs with Sphere Models

5.2.1. Dataset Generation. The simulation results in Section 5.1 are chosen to form the datasets for DNN. Therefore, the output of both model training and model testing is merely sound pressure. The differences between the datasets are the type and number of input variables. All input variables are generated with a normal distribution by the built-in random function. In order to avoid that the sound pressure distribution is not obvious due to excessive parameter changes, the maximum of the coefficient is 0.2, and the input variables change within a reasonable range. Table 2 lists all the parameters details. The 3σ principle is used to determine parameter variation ranges.

The datasets are specifically divided into two types: one with a single input is called "1-D" dataset, and the other with 5 inputs is called "5-D" dataset. These inputs are variables mentioned in Section 5.1 and also present in Table 2. The number of initial sampling points is 100 and 500 for 1-D and 5-D analysis, respectively. The calculation frequency is 50 Hz and 300 Hz because the numerical calculation method has high accuracy and the sound pressure changes smoothly at these two frequencies. The calculation point of the sound pressure is still at (5, 0, 0), which is outside the sphere and not at infinity.

According to equation (17), all inputs and outputs are standardized using built-in functions for DNN training and testing. The processed data conform to the standard normal distribution.

5.2.2. Model Training and Testing. Each dataset is automatically divided into training and testing datasets by a random process. Some training parameters are shown in Table 3. The ratio of the training set to test set is 9 : 1. The number of hidden layers for 1-D input and 5-D inputs is 2

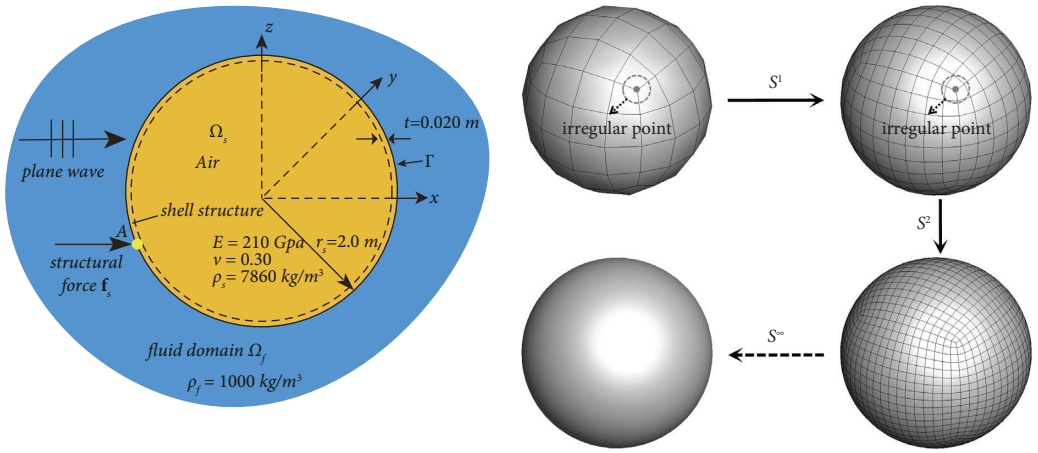

(a) (b)

FIGURE 9: The vibroacoustic coupling system: (a) the outside fluid is water; (b) Catmull–Clark subdivision surface is applied to subdivide the control mesh.

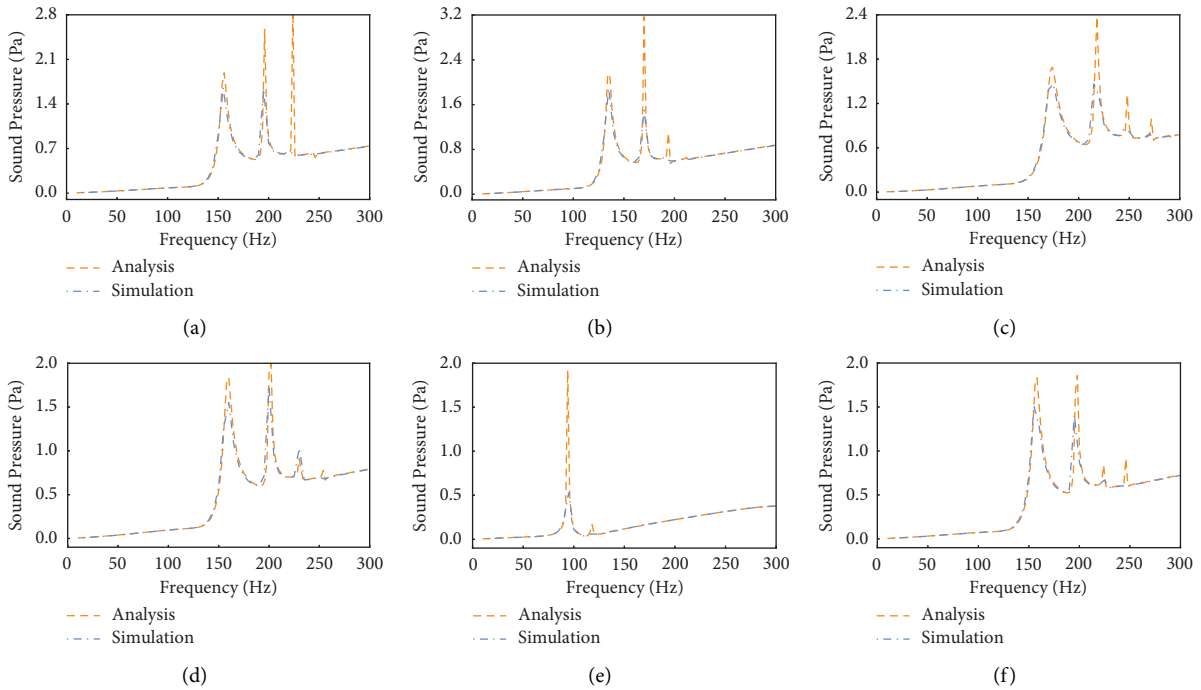

FIGURE 10: Comparison between analytical and numerical solutions of sound pressure with different variables for different frequencies. (a) Case 1. (b) Case 2. (c) Case 3. (d) Case 4. (e) Case 5. (f) Case 6.

TABLE 1: Variables setting for simulation verification.

Number	Radius (m)	Thickness (mm)	Density (kg/m^3)	Young's modulus (Pa)	Poisson ratio
Case 1	1.8	18	7860	$2.10E+11$	0.3
Case 2	2	18	7860	$2.10E+11$	0.3
Case 3	1.8	25	7860	$2.10E+11$	0.3
Case 4	1.8	18	6000	$2.10E+11$	0.3
Case 5	1.8	18	7860	$7.00E+10$	0.3
Case 6	1.8	18	7860	$2.10E+11$	0.2

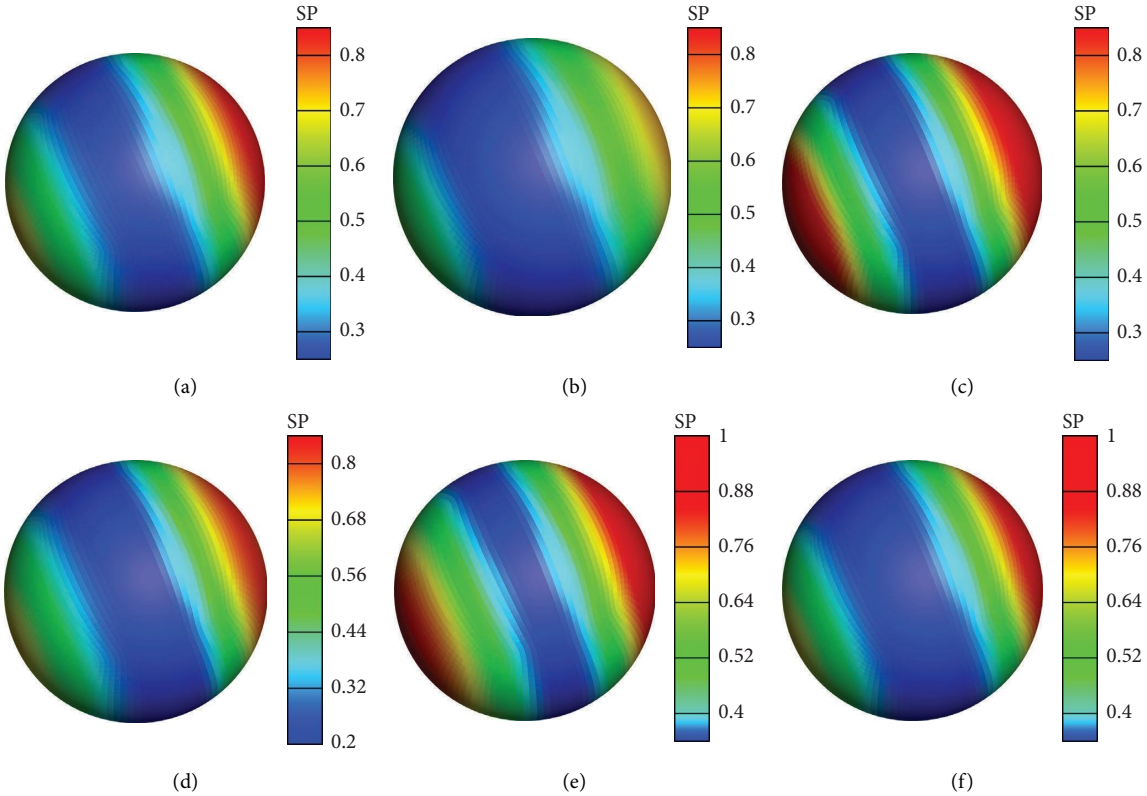

Figure 11: Spherical shell surface sound pressure distribution. (a) Case 1. (b) Case 2. (c) Case 3. (d) Case 4. (e) Case 5. (f) Case 6.

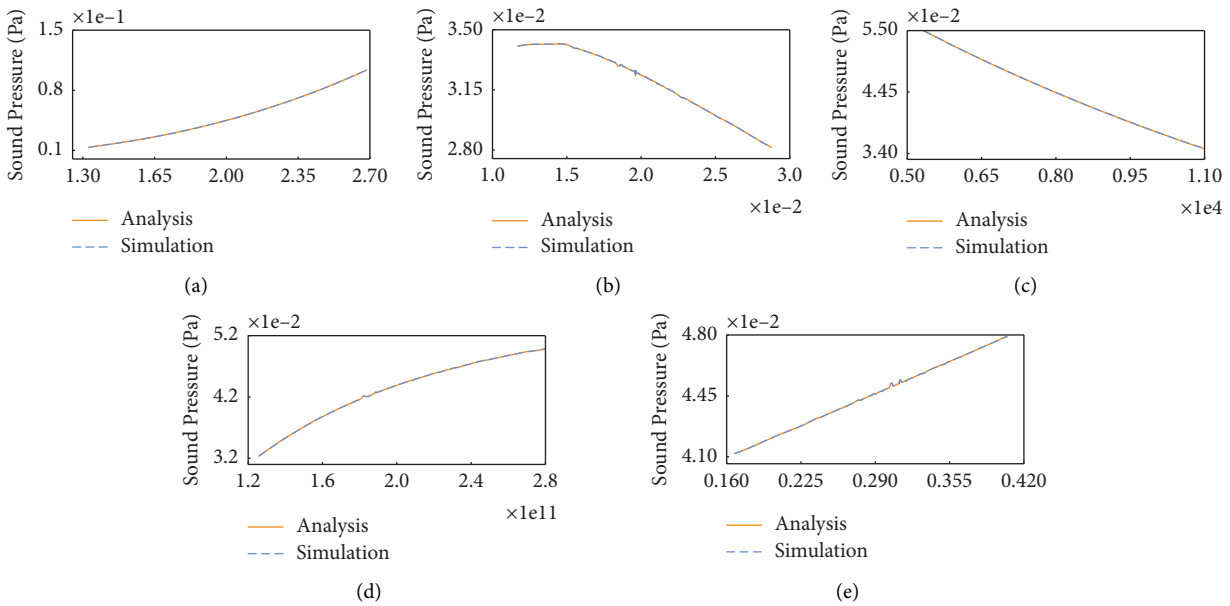

Figure 12: Sound pressure evolution with different variables at 50 Hz. (a) With radius (m). (b) With thickness (m). (c) With density (kg/m^3). (d) With Young's modulus (Pa). (e) With Poisson ratio.

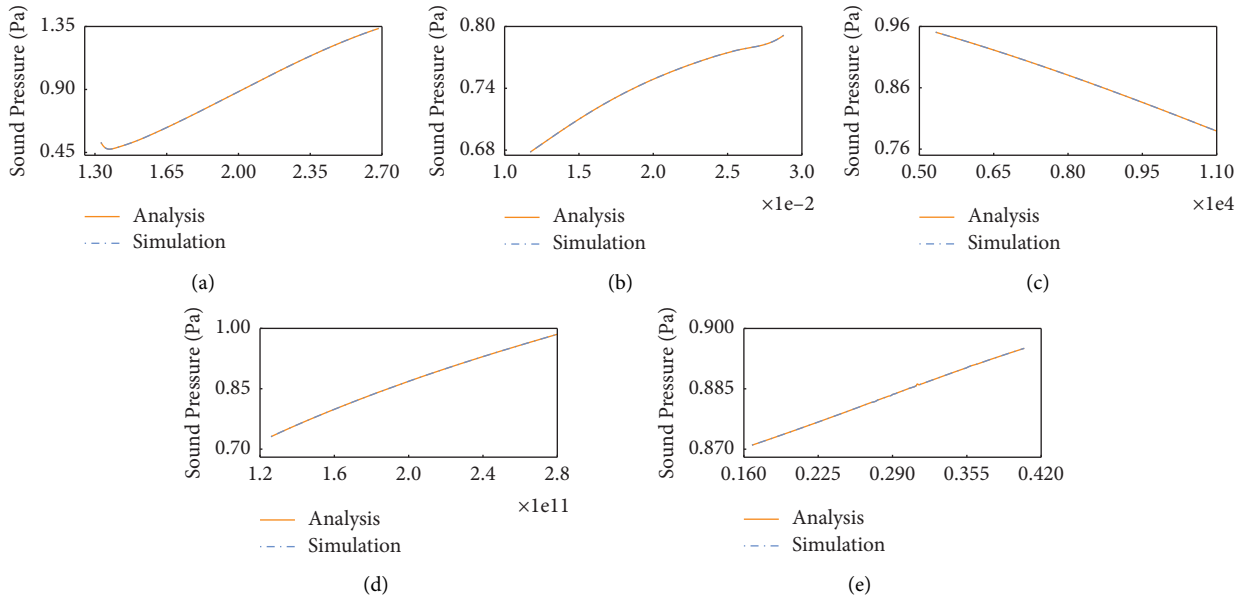

Figure 13: Sound pressure evolution with different variables at 300 Hz. (a) With radius (m). (b) With thickness (m). (c) With density (kg/m^3). (d) With Young's modulus (Pa). (e) With Poisson ratio.

Table 2: DNN training dataset input variable settings.

Variables	Mean	Variable boundary			
		$\gamma = 0.05$	$\gamma = 0.1$	$\gamma = 0.15$	$\gamma = 0.2$
Radius	2	(1.700, 2.300)	(1.400, 2.600)	(1.100, 2.900)	(0.800, 3.200)
Thickness	0.02	(0.017, 0.023)	(0.014, 0.026)	(0.011, 0.029)	(0.008, 0.032)
Density	7860	(6681, 9039)	(5502, 10218)	(4323, 11397)	(3144, 12576)
Young's modulus	$2.10E+11$	(1.785E11, 2.415E11)	(1.47E11, 2.73E11)	(1.155E11, 3.045E11)	(8.40E10, 3.36E11)
Poisson ratio	0.3	(0.255, 0.345)	(0.210, 0.390)	(0.165, 0.435)	(0.120, 0.480)

and 3, respectively. Since it is a simple regression problem, the optimizer is chosen as SGD. Different learning rates are picked for datasets of different dimensions. All processes are performed by an Intel(R) Xeon(R) Bronze 3204 CPU with PyTorch.

The loss function is MSE. Table 4 gives the loss change. For the 1-D input network, its loss converges faster than that of the 5-D input network (mainly because a bigger learning rate). Usually after 10 iterations, MSE can reach a quite low level for 1-D inputs, while the number of iterations is 100 for 5-D inputs. Finally, all losses have reached a low level, and all model training processes take less than 10 minutes.

For 1-D input and 5-D inputs, the prediction accuracies are verified by 10 and 50 data, respectively. Figures 14 and 15 give the comparison between the simulation and the DNN prediction at different frequencies. Except that in the comparison chart with shell thickness as a variable (Figures 14(b) and 15(b)) where there is a certain gap between the predicted results and the numerical calculation results in a small range, all of the rest of the subfigures show that the two solutions are in good agreement.

More specific statistical results calculated through equations (14)–(16) for DNN prediction evaluation are shown in Table 5 (all values are calculated after prediction destandardization), from which it could be found that the dispersion of prediction errors of each model is small and the model fits well to samples of different orders of magnitude. To sum up, the prediction effects of the trained models for different situations are good, and DNN can be used as an effective surrogate model to replace IGA FEM/BEM to generate samples.

5.2.3. MCs with Samples Generated by DNN. After obtaining a DNN model with a good fitting effect, it can be further utilized for uncertainty quantification analysis. Here, results of MCs with sound pressure generated by IGA FEM/BEM are used as a comparison. Table 6 shows the details for this. The new input data are also generated through the 3σ principle. For one-dimensional input, N in equations (1) and (2) are 100 and 1,000 for IGA FEM/BEM and DNN, respectively. For five-dimensional inputs, N is 500 and 2000.

Table 6 shows that the results of DNN are consistent with the IGA FEM/BEM results. As for calculating time contrast, the time of 1-dimensional input (per group) and 5-dimensional inputs of the IGA FEM/BEM method is about 3 hours and 12 hours, respectively, while for DNN, the calculation time is less than 1 minute regardless of

Table 3: Training hyperparameter settings.

Dimensions	Variables	Sample amount		Hidden layers		Optimizer	
		Training	Testing	Amount	Neurons	Type	Learning rate
1-D	Radius	90	10	2	(10, 10)	SGD	0.001
1-D	Thickness	90	10	2	(10, 10)	SGD	0.001
1-D	Density	90	10	2	(10, 10)	SGD	0.001
1-D	Young's modulus	90	10	2	(10, 10)	SGD	0.001
1-D	Poisson ratio	90	10	2	(10, 10)	SGD	0.001
5-D	All five	450	50	3	(10, 10, 10)	SGD	0.00001

Table 4: Training loss evolution.

Frequency (Hz)	Variables	Loss (MSE) with different iterations			
		10 iters	50 iters	100 iters	500 iters
50	1-D radius	$3.14E-02$	$1.03E-03$	$4.96E-03$	$4.41E-04$
	1-D thickness	$5.08E-03$	$8.85E-04$	$1.01E-02$	$6.22E-04$
	1-D density	$1.87E-03$	$1.17E-04$	$2.21E-04$	$2.59E-05$
	1-D Young's modulus	0.1389	$3.41E-03$	$2.46E-03$	$5.31E-04$
	1-D Poisson ratio	$9.99E-03$	$1.16E-03$	$5.15E-04$	$2.06E-04$
	5-D variables	2.4763	$3.62E-02$	0.1486	$2.05E-02$
300	1-D radius	$2.41E-02$	$2.01E-02$	$5.49E-04$	$1.37E-03$
	1-D thickness	0.1335	$8.63E-04$	$3.73E-04$	$8.52E-04$
	1-D density	$1.81E-03$	$1.55E-04$	$8.31E-05$	$2.07E-04$
	1-D Young's modulus	$4.87E-03$	$4.71E-04$	$2.39E-04$	$1.30E-03$
	1-D Poisson ratio	$2.71E-02$	$9.38E-04$	$3.20E-04$	$4.21E-04$
	5-D variables	6.5665	1.4078	0.3623	0.1480

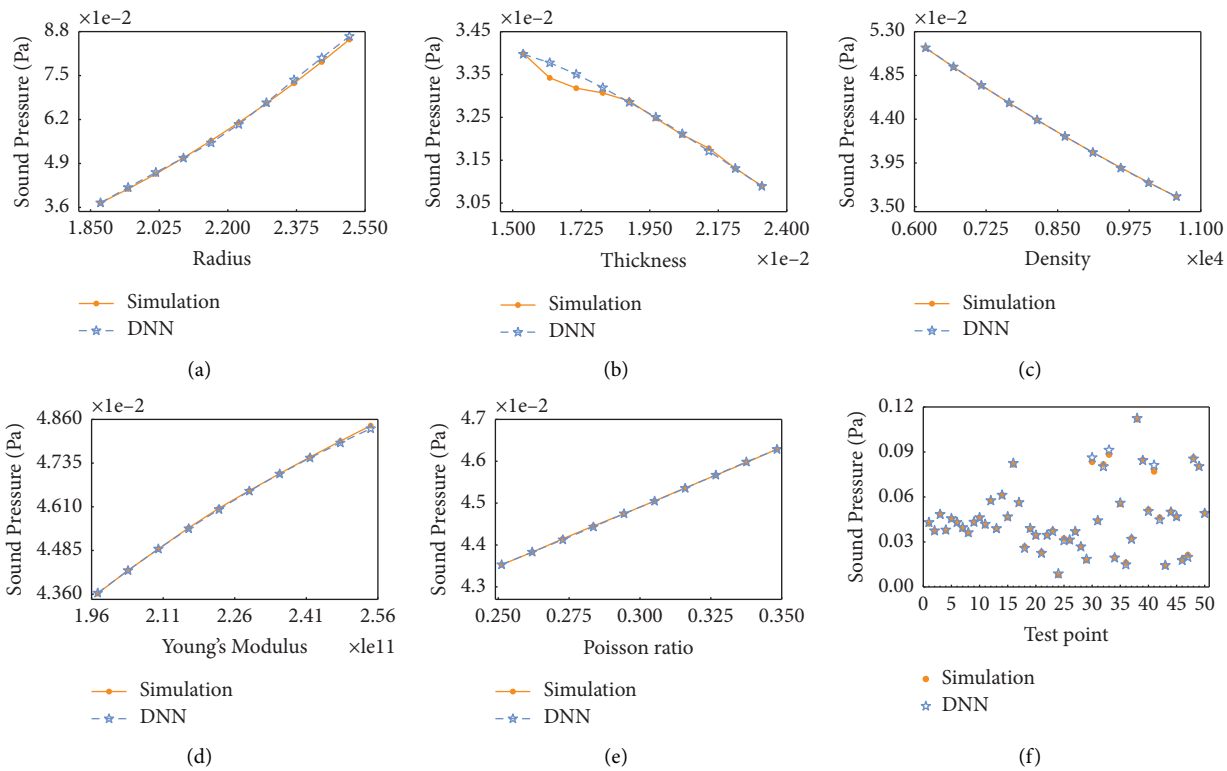

Figure 14: Comparison between simulation results and DNN prediction with different variables at 50 Hz. (a) With radius (m). (b) With thickness (m). (c) With density (kg/m^3). (d) With Young's modulus (Pa). (e) With Poisson ratio. (f) With 5 inputs.

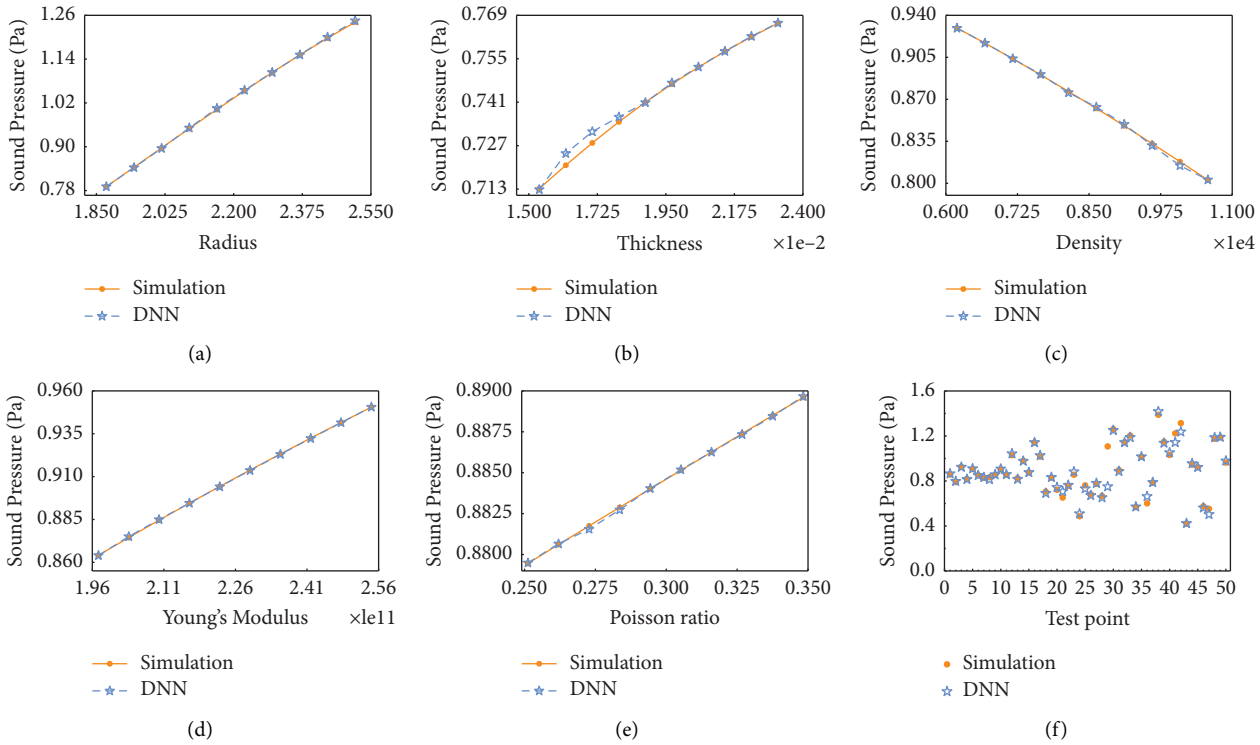

Figure 15: Comparison between simulation results and DNN prediction with different variables at 300 Hz. (a) With radius (m). (b) With thickness (m). (c) With density (kg/m^3). (d) With Young's modulus (Pa). (e) With Poisson ratio. (f) With 5 inputs.

Table 5: DNN prediction statistical results.

Frequency (Hz)	Variables	RMSE	MAE	MAPE
50	1-D radius	$7.17E-04$	$6.14E-04$	1.02
	1-D thickness	$1.24E-05$	$9.16E-06$	$2.82E-02$
	1-D density	$1.94E-05$	$1.72E-05$	$3.91E-02$
	1-D Young's modulus	$3.59E-05$	$2.78E-05$	$5.94E-02$
	1-D Poisson ratio	$6.74E-06$	$4.71E-06$	$1.05E-02$
	5-D variables	$1.04E-03$	$6.86E-04$	1.80
300	1-D radius	$2.13E-03$	$1.77E-03$	0.17
	1-D thickness	$1.89E-04$	$1.58E-04$	$2.12E-02$
	1-D density	$3.19E-04$	$2.26E-04$	$2.58E-02$
	1-D Young's modulus	$1.44E-04$	$1.05E-04$	$1.17E-02$
	1-D Poisson ratio	$6.49E-05$	$4.92E-05$	$5.57E-03$
	5-D variables	$5.59E-02$	$2.20E-02$	2.44

Table 6: MCs results of simulation and DNN.

Frequency (Hz)	Variables	Expectation		Standard deviation	
		Simulation	DNN	Simulation	DNN
50	1-D radius	$4.54E-02$	$4.67E-02$	$1.60E-02$	$1.72E-02$
	1-D thickness	$3.23E-02$	$3.23E-02$	$1.04E-03$	$1.11E-03$
	1-D density	$4.51E-02$	$4.52E-02$	$3.76E-03$	$4.00E-03$
	1-D Young's modulus	$4.44E-02$	$4.46E-02$	$3.05E-03$	$2.87E-03$
	1-D Poisson ratio	$4.49E-02$	$4.49E-02$	$1.11E-03$	$1.16E-03$
	5-D variables	$4.57E-02$	$4.64E-02$	$1.83E-02$	$1.90E-02$
300	1-D radius	$8.71E-01$	$8.81E-01$	$1.75E-01$	$1.85E-01$
	1-D thickness	$7.47E-01$	$7.47E-01$	$1.74E-02$	$1.78E-02$
	1-D density	$8.84E-01$	$8.85E-01$	$3.00E-02$	$3.05E-02$
	1-D Young's modulus	$8.80E-01$	$8.83E-01$	$4.56E-02$	$4.44E-02$
	1-D Poisson ratio	$8.85E-01$	$8.85E-01$	$4.02E-03$	$4.18E-03$
	5-D variables	$8.88E-01$	$8.92E-01$	$1.78E-01$	$1.74E-01$

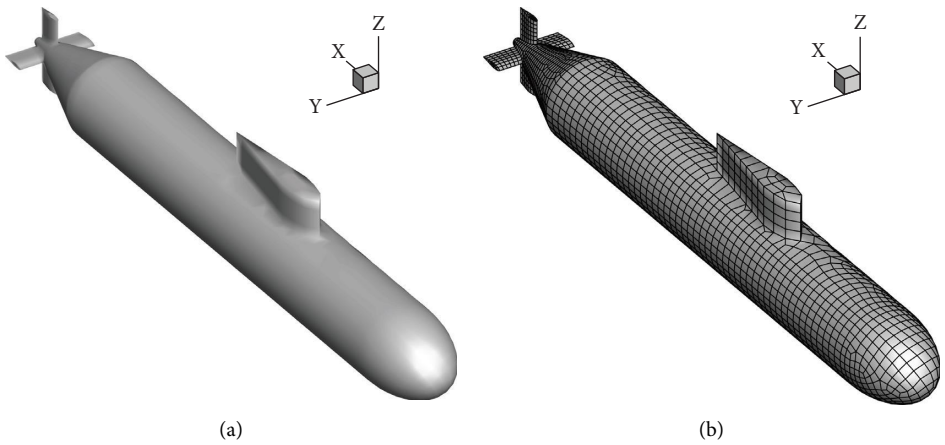

Figure 16: The submarine model (a) and its subdivision surface (b).

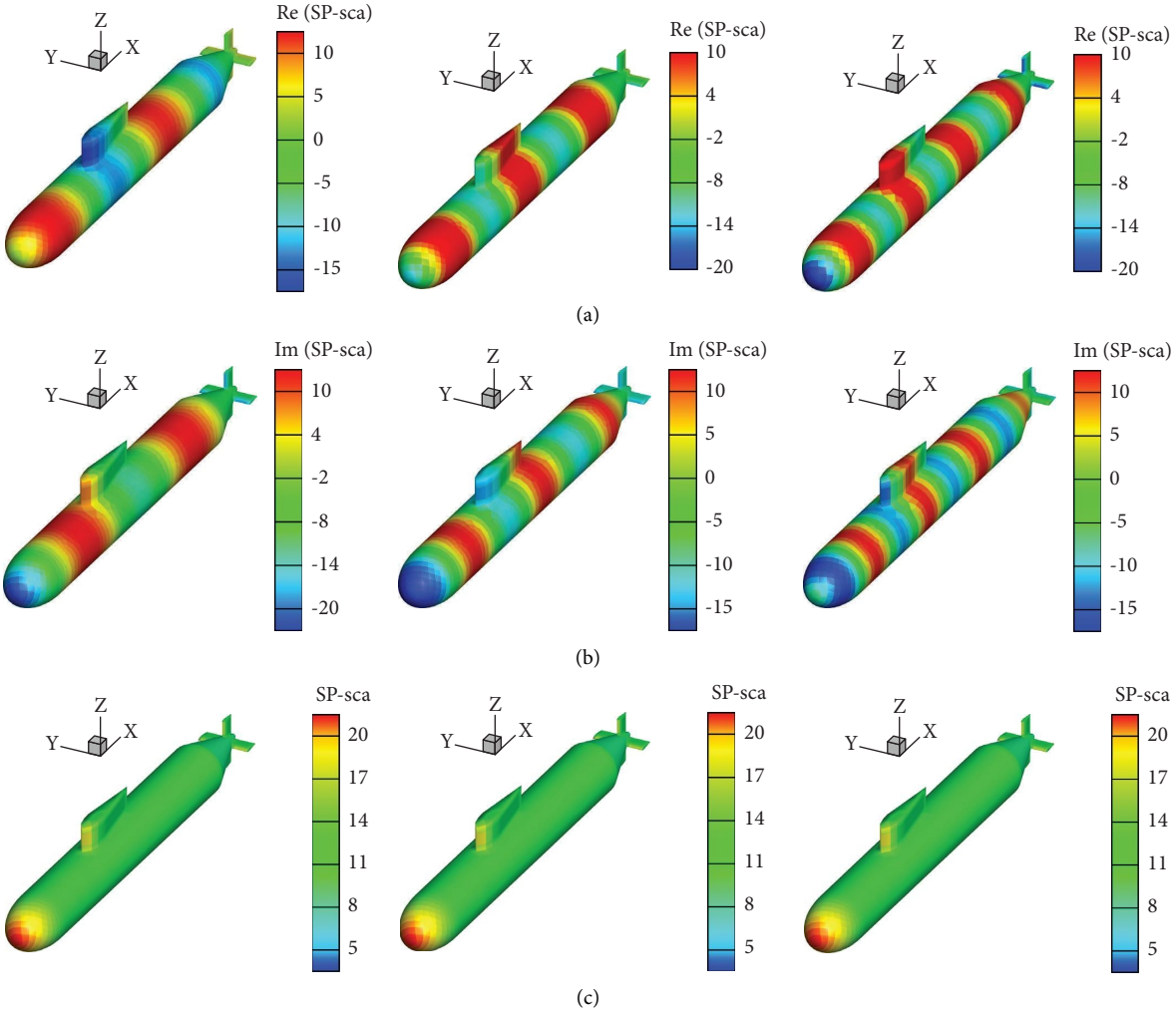

Figure 17: Sound pressure distribution at different frequencies (each picture from left to right in each part corresponds to 50 Hz, 75 Hz, and 100 Hz). (a) Real part. (b) Imaginary part. (c) Sound pressure.

dimensions (meanwhile, the amount of data is several times that of the numerical method). This shows the time advantage of DNN computing.

In conclusion, the DNN model is well-suited for uncertainty quantification, especially for multidimensional and large-scale inputs. The proposed method offers the

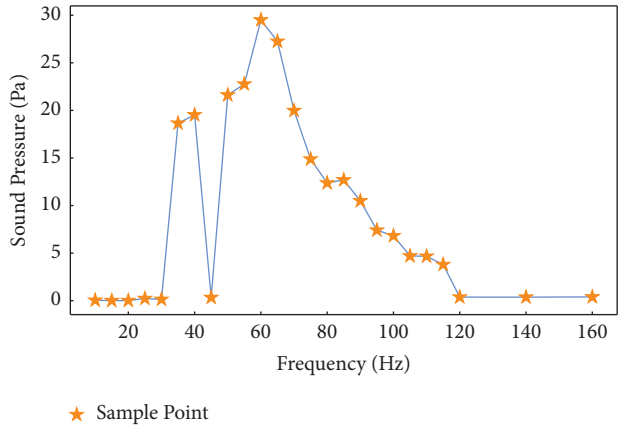

Figure 18: Sound pressure evolution.

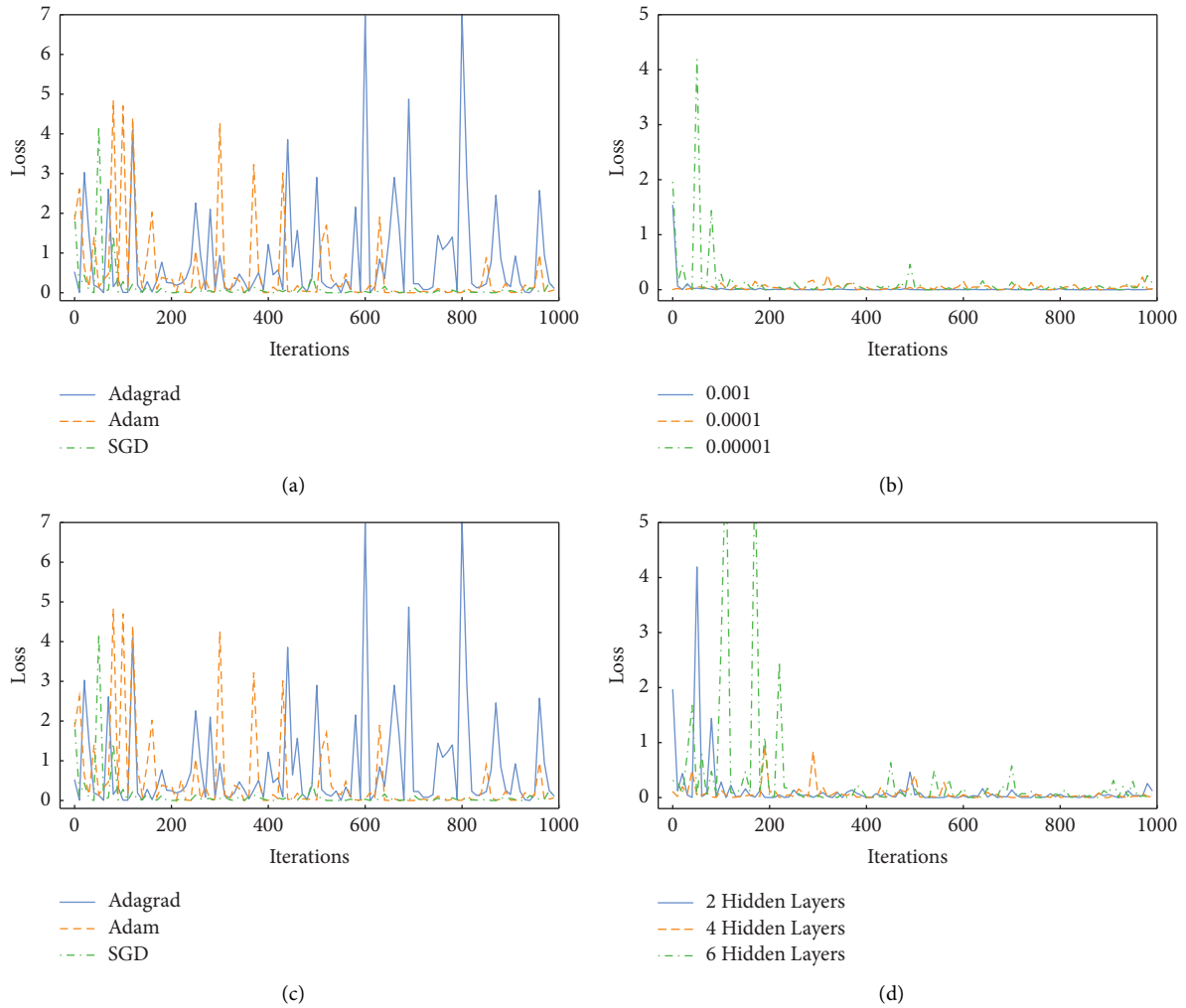

Figure 19: Training loss varies with different hyperparameters. (a) Different activation function. (b) Different learning rate. (c) Different optimizer. (d) Different amount of hidden layers.

advantage of eliminating the scale problem associated with the IGA FEM/BEM method and significantly reducing the calculation time.

5.3. DNN-MCs with the Complicated Model. The complicated thin-shell submarine model is used to prove the stochastic analysis ability of MCs with DNN in this section.

Table 7: DNN testing input parameters and results.

Test points	Thickness	Density	Young's modulus	Poisson ratio	Simulation	DNN	Relative error (%)
1	0.0536	8088.8471	$2.22E+11$	0.3111	8.0201	7.9639	0.70
2	0.0516	7550.6692	$1.99E+11$	0.3022	6.2470	6.3056	0.94
3	0.0507	8440.9587	$2.12E+11$	0.2782	6.5299	6.7278	3.03
4	0.0486	7730.0233	$2.08E+11$	0.2756	6.3238	6.3212	0.04
5	0.0507	7898.3327	$1.93E+11$	0.2812	4.0138	4.0400	0.65
6	0.0439	7489.9340	$1.67E+11$	0.2834	2.5693	2.3127	9.99
7	0.0514	6663.0713	$2.07E+11$	0.3318	7.6297	7.5717	0.76
8	0.0581	8242.2959	$1.81E+11$	0.2774	4.5975	4.7346	2.98
9	0.0413	7622.3172	$1.83E+11$	0.2652	2.6338	2.4841	5.68
10	0.0460	6730.4673	$2.17E+11$	0.2720	7.5994	7.3584	3.17
11	0.0384	6327.8107	$1.95E+11$	0.2717	3.5071	3.4159	2.60
12	0.0442	7610.9517	$1.71E+11$	0.3190	2.5558	2.5304	1.00
13	0.0433	7834.8434	$2.15E+11$	0.3558	4.3514	4.4192	1.56

The geometry model and its subdivision surface are shown in Figure 16. The loading conditions are similar to those of the sphere model. The response is calculated at fixed points (i.e., $m = 100$). DNN training data are still generated by IGA FEM/BEM, and numerical calculation result cloud diagrams are shown in Figure 17. It can be found that the sound pressure distribution varies across different frequencies. Figure 18 shows the evolution curve of sound pressure with frequency, from which we can see that 100 Hz is suitable for sampling. Because the sound pressure exhibits an obvious change and clear trend near this point, consequently, conducting calculations at this point can obtain data of higher quality.

For DNN training, the input variables are shell thickness, material density, Young's modulus, and Poisson ratio. The output value is sound pressure. All input variables are generated with a normal distribution by the built-in random function. The mean of four types of inputs is 0.05 m, 7860 kg/m^3, 210 GPa, and 0.3, respectively. The coefficients of variation for each variable include 0.05, 0.1, 0.015, and 0.2. 50 samples are generated through IGA FEM/BEM for each coefficient of variation.

Due to the complexity of the model, adjusting the hyperparameters of the DNN training process becomes necessary for achieving the optimal fitting network. Figure 19 shows how the training loss varies with different hyperparameters. Among different activation functions, tanh demonstrates faster convergence speed and avoids loss oscillation in later stages. As the learning rate decreases, the convergence speed of the model drops significantly, but the accuracy does not show a significant improvement. In comparison to the other two optimizers, despite not being the fastest in terms of convergence speed, SGD does not exhibit oscillation in later iterations, making it more effective overall. As the complexity of the model increases, the convergence speed initially rises and then declines, and the model with four hidden layers has the most favorable effect. Based on this, the activation function, learning rate, optimizer, and number of hidden layers of the trained DNN model are tanh, 0.01, SGD, and 4, respectively.

Table 7 shows the sound pressure comparison. For several points, the relative error is close to 10 percent, but for most points, the relative error is stable within 3 percent and mostly below 1 percent. This shows that the calculation results of the trained DNN surrogate model are in good agreement with the numerical simulation results.

Finally, the DNN model is used to generate 2000 datasets for MCs. Comparing the calculation time of IGA FEM/BEM with DNN, the former takes around 647.66 h, while the latter is only 18.7 s. This shows that DNN is far ahead of IGA FEM/BEM in efficiency. In the end, the expectation and standard deviation are calculated, and their values at the point (100, 0, 0) are 6.62 Pa and 3.21 Pa, respectively.

6. Conclusion

In this work, our purpose is to enhance the sampling speed of MCs and minimize the resource consumption of traditional numerical calculation methods. To achieve this, we utilize a DNN as a surrogate model to generate a substantial volume of multidimensional data. We employ the IGA FEM/BEM method to compute the sound pressure of the vibroacoustic coupling problem influenced by multidimensional uncertain parameters. Subsequently, we process these parameters and sound pressure values to construct the training dataset for DNN. The sound pressure predicted by DNN shows excellent agreement with the results of numerical calculations. Compared to IGA FEM/BEM, DNN also exhibits a significantly higher sample generation rate. This suggests that DNN holds great potential as a surrogate model. Furthermore, the MCs result comparison between DNN samples and numerical calculation samples is conducted, and the two match well, which affirms the effectiveness of the DNN surrogate model in performing stochastic analysis.

Data Availability

The data that support the findings of this study are available on request.

Conflicts of Interest

The authors declare that they have no conflicts of interest.

Acknowledgments

The authors appreciate the financial support of the National Natural Science Foundation of China (NSFC) under Grant no. 12102095.

References

[1] H. Arellano-Garcia, W. Martini, M. Wendt, and G. Wozny, "A new optimization framework for dynamic systems under uncertainty," *Computer Aided Chemical Engineering*, vol. 18, pp. 553–558, 2004.

[2] M. A. El-Gamal and E. Gamal, "A dynamic migration model with uncertainty," *Journal of Economic Dynamics and Control*, vol. 18, no. 3-4, pp. 511–538, 1994.

[3] M. Vorländer, "Computer simulations in room acoustics: concepts and uncertainties," *Journal of the Acoustical Society of America*, vol. 133, no. 3, pp. 1203–1213, 2013.

[4] L. Chen, H. Lian, Y. Xu et al., "Generalized isogeometric boundary element method for uncertainty analysis of time-harmonic wave propagation in infinite domains," *Applied Mathematical Modelling*, vol. 114, pp. 360–378, 2023.

[5] B. Han, D. Yin, and Y. Gao, "The application of a novel variable-order fractional calculus on rheological model for viscoelastic materials," *Mechanics of Advanced Materials and Structures*, pp. 1–13, 2023.

[6] Y. Gao, B. Zhao, M. Tang, and D. Yin, "Fractional modelling of salinity/temperature-dependent shear rheological behavior including stress overshoot for bentonite clay suspensions," *Applied Mathematical Modelling*, vol. 120, pp. 267–280, 2023.

[7] Z. Liu, P. Bian, Y. Qu et al., "A galerkin approach for analysing coupling effects in the piezoelectric semiconducting beams," *European Journal of Mechanics- A: Solids*, vol. 103, Article ID 105145, 2024.

[8] T. Tang and T. Zhou, "Recent developments in high order numerical methods for uncertainty quantification," *Science China Mathematics*, vol. 58, no. 7, p. 891, 07 2015.

[9] W. K. Hastings, "Monte Carlo sampling methods using Markov chains and their applications," *Biometrika*, vol. 57, no. 1, pp. 97–109, 1970.

[10] X. Shen, C. Du, S. Jiang, P. Zhang, and L. Chen, "Multivariate uncertainty analysis of fracture problems through model order reduction accelerated sbfem," *Applied Mathematical Modelling*, vol. 125, pp. 218–240, 2024.

[11] P. Glasserman, "Monte Carlo methods in financial engineering," *Monte Carlo Methods in Financial Engineering*, Springer Science & Business Media, Berlin, Germany, 2003.

[12] G. Evensen, "Sequential data assimilation with a nonlinear quasi-geostrophic model using Monte Carlo methods to forecast error statistics," *Journal of Geophysical Research: Oceans*, vol. 99, no. C5, pp. 10143–10162, 1994.

[13] H. Niederreiter, *Random Number Generation and Quasi-Monte Carlo Methods*, SIAM, Philadelphia, PA, USA, 1992.

[14] W. Chin, B. L. Marcolin, and P. R. Newsted, "A partial least squares latent variable modeling approach for measuring interaction effects. Results from a Monte Carlo simulation study and an electronic-mail emotion/adoption study," *Information Systems Research*, vol. 14, 2003.

[15] J. Biersack and L. Haggmark, "A Monte Carlo computer program for the transport of energetic ions in amorphous targets," *Nuclear Instruments and Methods*, vol. 174, no. 1-2, pp. 257–269, 1980.

[16] Y. M. Marzouk, H. N. Najm, and L. A. Rahn, *Stochastic Spectral Methods for Efficient Bayesian Solution of Inverse Problems*, American Institute of Physics, Maryland, MD, USA, 2005.

[17] P. L. T. Duong and M. Lee, "Uncertainty propagation in stochastic fractional order processes using spectral methods: a hybrid approach," *Communications in Nonlinear Science and Numerical Simulation*, vol. 17, no. 11, pp. 4262–4273, 2012.

[18] A. Ambrosetti and A. Malchiodi, *Perturbation Methods and Semilinear Elliptic Problems on R*, Birkhäuser Verlag, Basel, Switzerland, 2006.

[19] F. Ballio and A. Guadagnini, "Convergence assessment of numerical Monte Carlo simulations in groundwater hydrology," *Water Resources Research*, vol. 40, no. 4, 2004.

[20] J. Havinga, G. Klaseboer, and A. van den Boogaard, "Sequential optimization of strip bending process using multiquadric radial basis function surrogate models," *Key Engineering Materials*, vol. 554–557, pp. 911–918, 2013.

[21] M. Berkemeier and S. Peitz, "Derivative-free multiobjective trust region descent method using radial basis function surrogate models," 2021, https://arxiv.org/abs/2102.13444.

[22] K. Amouzgar, S. Bandaru, and A. H. C. Ng, "Radial basis functions with a priori bias as surrogate models: a comparative study," *Engineering Applications of Artificial Intelligence*, vol. 71, pp. 28–44, 2018.

[23] S. Zhang, B. Yu, and L. Chen, "Non-iterative reconstruction of time-domain sound pressure and rapid prediction of large-scale sound field based on ig-drbem and pod-rbf," *Journal of Sound and Vibration*, vol. 573, Article ID 118226, 2024.

[24] K. Kontolati, D. Loukrezis, K. R. M. dos Santos, D. G. Giovanis, and M. D. Shields, "Manifold learning-based polynomial chaos expansions for high-dimensional surrogate models," *International Journal for Uncertainty Quantification*, vol. 12, no. 4, pp. 39–64, 2022.

[25] N. Lüthen, S. Marelli, and B. Sudret, "A spectral surrogate model for stochastic simulators computed from trajectory samples," *Computer Methods in Applied Mechanics and Engineering*, vol. 406, Article ID 115875, 2023.

[26] K. Boopathy and M. P. Rumpfkeil, "Unified framework for training point selection and error estimation for surrogate models," *AIAA Journal*, vol. 53, no. 1, pp. 215–234, 2015.

[27] P. Chen, N. Zabaras, and I. Bilionis, "Uncertainty propagation using infinite mixture of Gaussian processes and variational bayesian inference," *Journal of Computational Physics*, vol. 284, pp. 291–333, 2015.

[28] V. Hombal and S. Mahadevan, "Bias minimization in Gaussian process surrogate modeling for uncertainty quantification," *International Journal for Uncertainty Quantification*, vol. 1, no. 4, pp. 321–349, 2011.

[29] S. Olofsson, M. P. Deisenroth, and R. Misener, "Design of experiments for model discrimination using Gaussian process surrogate models," *Computer Aided Chemical Engineering*, vol. 44, pp. 847–852, 2018.

[30] M. Y. Li, E. Grant, and T. L. Griffiths, "Gaussian process surrogate models for neural networks," 2022, https://arxiv.org/abs/2208.06028.

[31] I. Bilionis and N. Zabaras, "Multidimensional adaptive relevance vector machines for uncertainty quantification," *SIAM Journal on Scientific Computing*, vol. 34, no. 6, pp. B881–B908, 2012.

[32] C. Zhou, Z. Lu, and X. Yuan, "Use of relevance vector machine in structural reliability analysis," *Journal of Aircraft*, vol. 50, no. 6, pp. 1726–1733, 2013.

[33] G. Huang, G. Wu, Z. Yang, X. Chen, and W. Wei, "Development of surrogate models for evaluating energy transfer quality of high-speed railway pantograph-catenary system using physics-based model and machine learning," *Applied Energy*, vol. 333, Article ID 120608, p. 2023, 2023.

[34] M. Y. Jung, J. H. Chang, M. Oh, and C. H. Lee, "Dynamic model and deep neural network-based surrogate model to predict dynamic behaviors and steady-state performance of solid propellant combustion," *Combustion and Flame*, vol. 250, Article ID 112649, 2023.

[35] M. G. Kontou, V. G. Asouti, and K. C. Giannakoglou, "Dnn surrogates for turbulence closure in cfd-based shape optimization," *Applied Soft Computing*, vol. 134, Article ID 110013, 2023.

[36] M. Shahriari, D. Pardo, B. Moser, and F. Sobieczky, "A deep neural network as surrogate model for forward simulation of borehole resistivity measurements," *Procedia Manufacturing*, vol. 42, pp. 235–238, 2020.

[37] R. Sun, B. Pan, and Q. Duan, "A surrogate modeling method for distributed land surface hydrological models based on deep learning," *Journal of Hydrology*, vol. 624, Article ID 129944, 2023.

[38] X. Shen, C. Du, S. Jiang, L. Sun, and L. Chen, "Enhancing deep neural networks for multivariate uncertainty analysis of cracked structures by pod-rbf," *Theoretical and Applied Fracture Mechanics*, vol. 125, Article ID 103925, 2023.

[39] L. Chen, H. Li, Y. Guo, P. Chen, E. Atroshchenko, and H. Lian, "Uncertainty quantification of mechanical property of piezoelectric materials based on isogeometric stochastic fem with generalized nth-order perturbation," *Engineering with Computers*, 2023.

[40] H. Zhai, Q. Zhou, and G. Hu, "Predicting micro-bubble dynamics with semi-physics-informed deep learning," *AIP Advances*, vol. 12, no. 3, p. 2022, 2022.

[41] H. Ouyang, Z. Zhu, K. Chen, B. Tian, B. Huang, and J. Hao, "Reconstruction of hydrofoil cavitation flow based on the chain-style physics-informed neural network," *Engineering Applications of Artificial Intelligence*, vol. 119, Article ID 105724, 2023.

[42] J. Ostrometzky, K. Berestizshevsky, A. Bernstein, and G. Zussman, "Physics-informed deep neural network method for limited observability state estimation," 2019, https://arxiv.org/abs/1910.06401.

[43] L. Chen, Z. Wang, H. Lian et al., "Reduced order isogeometric boundary element methods for cad-integrated shape optimization in electromagnetic scattering," *Computer Methods in Applied Mechanics and Engineering*, vol. 419, Article ID 116654, 2024.

[44] L. Chen, J. Zhao, H. Lian, B. Yu, E. Atroshchenko, and P. Li, "A bem broadband topology optimization strategy based on taylor expansion and soar method—application to 2d acoustic scattering problems," *International Journal for Numerical Methods in Engineering*, vol. 124, no. 23, pp. 5151–5182, 2023.

[45] L. Chen, K. Li, X. Peng, H. Lian, X. Lin, and Z. Fu, "Isogeometric boundary element analysis for 2dtransientheat conduction problem with radial integration method," *Computer Modeling in Engineering and Sciences*, vol. 126, no. 1, pp. 125–146, 2021.

[46] L. Chen, H. Lian, S. Natarajan, W. Zhao, X. Chen, and S. Bordas, "Multi-frequency acoustic topology optimization of sound-absorption materials with isogeometric boundary element methods accelerated by frequency-decoupling and model order reduction techniques," *Computer Methods in Applied Mechanics and Engineering*, vol. 395, Article ID 114997, p. 2022, 2022.

[47] C. Lu, L. Chen, J. Luo, and H. Chen, "Acoustic shape optimization based on isogeometric boundary element method with subdivision surfaces," *Engineering Analysis with Boundary Elements*, vol. 146, pp. 951–965, 2023.

[48] G. Cao, B. Yu, L. Chen, and W. Yao, "Isogeometric dual reciprocity bem for solving non-fourier transient heat transfer problems in fgms with uncertainty analysis," *International Journal of Heat and Mass Transfer*, vol. 203, Article ID 123783, 2023.

[49] L. Chen, Z. Wang, X. Peng, J. Yang, P. Wu, and H. Lian, "Modeling pressurized fracture propagation with the isogeometric bem," *Geomechanics and Geophysics for Geo-Energy and Geo-Resources*, vol. 7, no. 3, p. 51, 2021.

[50] G. C. Everstine and F. M. Henderson, "Coupled finite element/boundary element approach for fluid-structure interaction," *Journal of the Acoustical Society of America*, vol. 87, no. 5, pp. 1938–1947, 1990.

[51] T. J. R. Hughes, J. A. Cottrell, and Y. Bazilevs, "Isogeometric analysis: CAD, finite elements, NURBS, exact geometry and mesh refinement," *Computer Methods in Applied Mechanics and Engineering*, vol. 194, no. 39-41, pp. 4135–4195, 2005.

[52] H. Lian, P. Kerfriden, and S. Bordas, "Implementation of regularized isogeometric boundary element methods for gradient-based shape optimization in two-dimensional linear elasticity," *International Journal for Numerical Methods in Engineering*, vol. 106, no. 12, pp. 972–1017, 2016.

[53] H. Lian, P. Kerfriden, and S. P. A. Bordas, "Shape optimization directly from cad: an isogeometric boundary element approach using T-splines," *Computer Methods in Applied Mechanics and Engineering*, vol. 317, pp. 1–41, 2017.

[54] L. Chen, C. Lu, H. Lian et al., "Acoustic topology optimization of sound absorbing materials directly from subdivision surfaces with isogeometric boundary element methods," *Computer Methods in Applied Mechanics and Engineering*, vol. 362, Article ID 112806, 2020.

[55] L. Chen, R. Cheng, S. Li, H. Lian, C. Zheng, and S. P. A. Bordas, "A sample-efficient deep learning method for multivariate uncertainty qualification of acoustic–vibration interaction problems," *Computer Methods in Applied Mechanics and Engineering*, vol. 393, Article ID 114784, 2022.

[56] W. Zhao, L. Chen, H. Chen, and S. Marburg, "Topology optimization of exterior acoustic-structure interaction systems using the coupled fem-bem method," *International Journal for Numerical Methods in Engineering*, vol. 82, 2019.

[57] L. Chen, H. Lian, Z. Liu, Y. Gong, C. Zheng, and S. P. A. Bordas, "Bi-material topology optimization for fully coupled structural-acoustic systems with isogeometric fem–bem," *Engineering Analysis with Boundary Elements*, vol. 135, pp. 182–195, 2022.

[58] Q. Magazine, *New Theory Cracks Open the Black Box of Deep Learning*, The MIT Press, Cambridge, MA, USA, 2017.

[59] Y. Wang, Z. Liao, S. Shi, Z. Wang, and L. Hien Poh, "Data-driven structural design optimization for petal-shaped auxetics using isogeometric analysis," *Computer Modeling in Engineering and Sciences*, vol. 122, no. 2, pp. 433–458, 2020.

[60] A. Oishi and G. Yagawa, "Computational mechanics enhanced by deep learning," *Computer Methods in Applied Mechanics and Engineering*, vol. 327, pp. 327–351, 2017.

[61] Y. Levine, N. Wies, O. Sharir, N. Cohen, and A. Shashua, "Tensors for deep learning theory," *Tensors for Data*

Processing, pp. 215–248, Elsevier Science, Amsterdam, Netherlands, 2022.

[62] L. Chen, Y. Zhang, H. Lian, E. Atroshchenko, C. Ding, and S. Bordas, "Seamless integration of computer-aided geometric modeling and acoustic simulation: isogeometric boundary element methods based on catmull-clark subdivision surfaces," *Advances in Engineering Software*, vol. 149, Article ID 102879, 2020.

[63] Z. Liu, M. Majeed, F. Cirak, and R. N Simpson, "Isogeometric fem-bem coupled structural-acoustic analysis of shells using subdivision surfaces," *International Journal for Numerical Methods in Engineering*, vol. 113, no. 9, pp. 1507–1530, 2018.

[64] H. Lian, L. Chen, X. Lin, W. Zhao, S. P A Bordas, and M. Zhou, "Noise pollution reduction through a novel optimization procedure in passive control methods," *Computer Modeling in Engineering and Sciences*, vol. 131, no. 1, pp. 1–18, 2022.

[65] A. J. Burton, G. F. Miller, and J. H. Wilkinson, "The application of integral equation methods to the numerical solution of some exterior boundary-value problems," *Proceedings of the Royal Society of London A Mathematical and Physical Sciences*, vol. 323, no. 1553, pp. 201–210, 1971.

[66] S. Marburg, "The burton and miller method: unlocking another mystery of its coupling parameter," *Journal of Computational Acoustics*, vol. 24, no. 01, Article ID 1550016, 2016.

[67] S. Marburg, "Developments in structural-acoustic optimization for passive noise control," *Archives of Computational Methods in Engineering*, vol. 9, no. 4, pp. 291–370, 2002.

[68] L. Chen, H. Lian, Z. Liu, H. Chen, E. Atroshchenko, and S. P. A. Bordas, "Structural shape optimization of three dimensional acoustic problems with isogeometric boundary element methods," *Computer Methods in Applied Mechanics and Engineering*, vol. 355, pp. 926–951, 2019.

[69] L. Chen, C. Liu, W. Zhao, and L. Liu, "An isogeometric approach of two dimensional acoustic design sensitivity analysis and topology optimization analysis for absorbing material distribution," *Computer Methods in Applied Mechanics and Engineering*, vol. 336, pp. 507–532, 2018.

[70] L. Chen, C. Lu, W. Zhao, H. Chen, and C. Zheng, "Subdivision surfaces— boundary element accelerated by fast multipole for the structural acoustic problem," *Journal of Theoretical and Computational Acoustics*, vol. 28, no. 02, Article ID 2050011, 2020.

[71] N. Nishimura, "Fast multipole accelerated boundary integral equation methods," *Applied Mechanics Reviews*, vol. 55, no. 4, pp. 299–324, 2002.

[72] T. Takahashi and T. Matsumoto, "An application of fast multipole method to isogeometric boundary element method for laplace equation in two dimensions," *Engineering Analysis with Boundary Elements*, vol. 36, no. 12, pp. 1766–1775, 2012.

[73] R. N. Simpson and Z. Liu, "Acceleration of isogeometric boundary element analysis through a black-box fast multipole method," *Engineering Analysis with Boundary Elements*, vol. 66, pp. 168–182, 2016.